DESIGN AND OPTIMIZATION OF AN InGaP/GaAs/Si$_X$Ge$_{1-X}$ SOLAR CELL CONSIDERING RECOMBINATION EFFECTS

A thesis submitted to the

Department of Electrical and Electronic Engineering
Bangladesh University of Engineering and Technology (BUET)

by

Sayema Chowdhury

In partial fulfillment of the requirement for the degree of
Master of Science in Electrical and Electronic Engineering

DEPARTMENT OF ELECTRICAL AND ELECTRONIC ENGINEERING
BANGLADESH UNIVERSITY OF ENGINEERING AND TECHNOLOGY(BUET)
DHAKA-1000, BANGLADESH

August 2015

Certification

The thesis titled **"DESIGN AND OPTIMIZATION OF AN InGaP/GaAs/Si_XGe_{1-X} SOLAR CELL CONSIDERING RECOMBINATION EFFECTS"** submitted by Sayema Chowdhury, Student No: 0412062257, Session: April, 2012, has been accepted as satisfactory in partial fulfillment of the requirement for the degree of MASTER OF SCIENCE IN ELECTRICAL AND ELECTRONIC ENGINEERING on August 1, 2015.

BOARD OF EXAMINERS:

1.	Dr. Md. Nasim Ahmed Dewan Professor Dept. of EEE, BUET, Dhaka-1000.	Chairman (Supervisor)
2.	Head of the Department Dept. of EEE, BUET, Dhaka-1000.	Member (Ex-Officio)
3.	Dr. Quazi Deen Mohd Khosru Professor Dept. of EEE, BUET, Dhaka-1000.	Member
4.	Dr. Md. Anwarul Abedin Professor Department of EEE DUET, Gazipur	Member (External)

CANDIDATES DECLARATION

This is to certify that the work presented in this thesis titled **“DESIGN AND OPTIMIZATION OF AN InGaP/GaAs/Si$_X$Ge$_{1-X}$ SOLAR CELL CONSIDERING RECOMBINATION EFFECTS**” is the outcome of the study carried out by me under the supervision of Dr. Md. Nasim Ahmed Dewan. It is also declared that neither this thesis nor any part thereof has not been submitted or is being currently submitted elsewhere for the award of any degree or diploma.

Signature of the Candidate

____

Sayema Chowdhury **Author**
Student ID: 0412062257
Session: April 2012

Countersign

____

Dr. Md. Nasim Ahmed Dewan **Supervisor**
Professor
Dept. of EEE, BUET
Dhaka-1000.

ABSTRACT

Multi-junction III–V solar cells for terrestrial and space applications have attracted increasing attention in recent years for their very high conversion efficiencies. However, increasing the efficiency while maintaining the cost within certain limits, still remains a big challenge for present day researchers. Much work has been done for solar cells under ideal conditions and concentrated sun, but a detailed study considering non idealities such as recombination effects is still missing. Currently, state-of-the-art high efficiency III–V solar cells utilize a three-junction design that includes a Ge bottom junction formed in the Ge substrate in conjunction with lattice-matched $Ga_{0.5}In_{0.5}P$ and GaAs top junctions. Such a structure is limited by the lattice matching constraint and hence does not offer many choices of materials. One way around is to use a mechanically stacked configuration which will remove the problem for lattice matching, at the same time reducing cost. In this thesis, the compound semiconductor Si_xGe_{1-x} is used for the first time as the bottom cell material and its composition is varied to obtain maximum efficiency for a particular composition. Also non ideal effects such as surface recombination, Shockley Reed Hall recombination and Auger recombination are all considered in the study. To start off $Si_{0.11}Ge_{0.89}$ was selected for bottom cell and for this, the I-V characteristics were studied. Later, the thicknesses of the layers were varied and its effects were seen on the overall short circuit current and efficiency. It was observed that as the top cell thickness was increased, the top cell short circuit current also increased, but the middle cell short circuit current significantly decreased due to shadowing effect. Again, with the increase in middle cell thickness, the middle cell short circuit current was found to increase. Thus an optimum thickness was chosen for the best possible efficiency. For $Si_{0.65}Ge_{0.35}$ bottom cell composition, top cell thickness of 0.4µm and middle cell thickness of 4µm, highest efficiency of 32.2% was obtained. This structure is then further optimized by changing the thickness of the additional layers that are used to minimize losses and enhance device performance, such as the window layer, back surface field (BSF) layer. For a window layer thickness of 0.01µm and BSF layer thickness of 0.02µm, maximum efficiency of 34.85% was obtained. Finally for this optimized structure, an efficiency of 41.34% was achieved under ideal conditions.

CONTENTS

LIST OF FIGURES

LIST OF TABLES

Chapter 1

INTRODUCTION

1.1 Preface

A history of photovoltaics goes back to 1839, when Edmund Becquerel observed a photovoltaic effect in liquid electrolytes [1]. However it was not until 1954 that the first solar cell was developed at Bell Laboratories with an efficiency of 6% [2]-[3]. Since then, much research has been done in the field of photovoltaics that resulted in various different types of solar cells, which can broadly be classified into three generations.

The first generation of solar cells, also known as silicon wafer-based photovoltaic, is the dominant technology for terrestrial applications today, accounting for more than 85% of the solar cell market. These cells offer power conversion efficiencies up to 25%, although the fabrication technologies at present limit them to about 15 to 20% [4].

Second-generation materials are based on the use of “thin-film” deposits of semiconductors, such as amorphous silicon or cadmium telluride. Even though these second-generation thin film cells are typically less efficient (efficiencies around 6% to 10%) than first generation silicon cells, the lower costs in manufacturing has achieved a lower cost per watt. Besides, decreased mass allows fitting panels on light materials or flexible materials, even textiles.

Increasing the efficiency of the second generation solar cells, maintaining the cost advantage however, is the primary goal of the third generation solar cells. Several advancements have been made in this research field, some of which are dye sensitized nanocrystalline or Gratzel solar cells, organic polymer-based photovoltaics, tandem (or multi-junction) solar cells, hot carrier solar cells, multi-band and thermo photovoltaic solar cells. Among these, the Multi junction solar cell is gaining increasing attention in recent years. The solar radiation is a broadly distributed energy resource, and to exploit the solar spectrum more profitably, multiple cells having different bandgaps are connected in series to divide the broad spectrum into smaller sections each of which can be converted to electricity more efficiently [5]-[11]. This is the main working principle of a multi junction solar cell.

1.2 Literature Review

GaAs and Ge lattice-matched semiconductor compounds were originally used to fabricate dual junction solar cells [12]-[13]. With the addition of an active Ge subcell, upright 3-junction solar cells with both lattice-matched and metamorphic InGaP/(In)GaAs/Ge designs have achieved over 40% efficiency [14]-[15]. These designs have achieved 41.6% efficiency under 364 suns for lattice-matched cells [16]. However, the Ge junction absorbs approximately two times more low energy photons than are needed for current matching with the $Ga_{0.5}In_{0.5}P$ and GaAs junctions and hence Current-matching for such cells is a major constraint for further improvement of efficiencies. Ideally, the Ge bottom junction would be replaced with a 1.0 eV junction that is lattice matched with the other junctions [17].The dilute nitride alloy $Ga_xIn_{1-x}N_yAs_{1-y}$ initially appeared to satisfy these requirements, To date, the world record 3-junction solar cell (43.5% under 418-suns illumination) utilizes this alloy as the middle 1eV subcell, allowing for a better current match between the different subcells. One promising combination of III-V direct band gap semiconductor materials is based on InP lattice constant[18]-[20] but the dilute nitride alloys are proved to be limited by what appears to be intrinsic defects [21]. $In_{0.3}Ga_{0.7}As$ could also be used as the 1.0 eV junction, but it has a larger lattice constant than GaAs by about 2% [15]. The strain resulting from the lattice misfit in these designs is enough to generate numerous dislocations that significantly degrades device performance. The dislocations generated by this large lattice mismatch (LMM) can be reduced through the use of graded composition buffer layers [22]-[23] sometime referred to as “metamorphic” growth, but the remaining threading dislocations would significantly degrade any subsequently grown junctions with higher band gaps. One way around this limitation is an inverted metamorphic multijunction (IMM) design [24]-[25], which enables better band gap energy combinations. Many research studies have investigated the promise of metamorphic materials for solar cells [26]-[33]. Recently, an IMM approach achieved 43.5% under concentrated sunlight by using a combination of InGaP/GaAs/InGaAs subcells. In this scheme, it is necessary to remove the substrate after growth to permit the incident sunlight to enter the ‘‘top” (i.e., the high-bandgap junction) of the cell [15].However, further improvements will still likely be limited by threading dislocations because of the lattice-mismatch. These constraints on compatible materials systems can be bypassed by removing the requirement that all the junctions in the multijunction structure be grown monolithically. Instead, in this approach, the different junctions are grown separately and then either bonded or mechanically stacked together. Atwater and coworkers [34]-[35], have combined bonding with ion-induced layer transfer in working toward the development of a practical, high-performance bonded multijunction cell. However, several defects are introduced in such a method. Another way to mechanically stack the layers is to use adhesive layers in between junctions. We propose a mechanically stacked triple junction solar cell that uses the compound semiconductor SiGe as the bottom cell, eradicating the need for lattice matching since it uses adhesive layers to connect the cells in series.Moreover, the use of SiGe material as the bottom cell gives us an oppurtunity to engineer the bandgap and bring it close to 1eV significantly imroving the current matching and hence the overall cell performance. A detailed physics based analysis of cell parameters considering non ideal effects is yet to be done.

1.3 Thesis Objective

The Primary objective of this work is to design a mechanically stacked triple junction solar cell based on SiGe bottom cell considering non ideal conditions i.e. surface recombination, Auger recombination and Shockley-Reed-Hall recombination. Next the bandgap of bottom cell material will be engineered by changing SiGe alloy composition and to analyze effect on cell performance. In this work, the $Si_{0.11}Ge_{0.89}$ alloy will be used as a starting point and the composition will then be varied and the cell performance will be analyzed. Next, the cell efficiency will be studied as a function of emitter and base thicknesses. Finally window layer thickness and back surface layer thickness will be altered and its effect on cell performance will be seen.

1.4 Thesis Organization:

This thesis is divided into four chapters and one reference

- The review of solar cell technology and the current status of similar research work have been described in chapter 1.
- In chapter 2, the theory of operation of a solar cell, the detailed methods of analysis of solving drift diffusion current is given. Also the computational details are discussed at the end of chapter 2
- Chapter 3 deals with the results and discussions. A detailed discussion of the results is carried out and finally the solar cell is optimized.
- Chapter 4 presents the conclusion of the study.

Chapter 2

THEORY

2. 1 Introduction

In this chapter different types of solar cells are discussed at first and then the basic working principle of a p-n junction solar cell is explained, highlighting the key parameters and loss mechanisms. Next, detailed numerical analysis is carried out to solve the drift diffusion current equation used in simulation of the solar cells in Silvaco ATLAS. Lastly detailed computational methods of ATLAS are discussed.

2. 2 Solar Cell

A solar cell, or photovoltaic cell, is an electrical device that converts the energy of light directly into electricity by the photovoltaic effect. It is a form of photoelectric cell, defined as a device whose electrical characteristics, such as current, voltage, or resistance, vary when exposed to light. Solar cells are the building blocks of photovoltaic modules, otherwise known as solar panels.

2. 2.1 Types:

Solar cells are of different types. Some of the notable ones are discussed below:

a) **Amorphous silicon solar cell (a-Si):** Its basic electronic structure is the p-i-n junction. a-Si is attractive as a solar cell material because it's an abundant, non-toxic material

b) **Bio hybrid solar cell:** A bio hybrid solar cell is a solar cell made using a combination of organic matter (photo system I) and inorganic matter. Multiple layers of photo system I gather photonic energy, convert it into chemical energy and create a current that goes through the cell.

c) **Cadmium telluride solar cell (CdTe):**Cadmium telluride (CdTe) photovoltaic describes a photovoltaic (PV) technology that is based on the use of cadmium telluride, a thin semiconductor layer designed to absorb and convert sunlight into electricity. Cadmium telluride PV is the only thin film technology with lower costs than conventional solar cells made of crystalline silicon in multi-kilowatt systems [36]-[38].

d) **Crystalline silicon solar cell (c-Si):** Solar cells made of crystalline silicon are often called *conventional*, *traditional*, or *first generation* solar cells, as they were developed in the 1950s and remained the most common type up to the present time [2]. Because they are produced from about 160 µm thick solar wafers—slices from bulks of solar grade silicon—they are sometimes called *wafer-based* solar cells.

e) **Organic solar cell:** An organic solar cell or plastic solar cell is a type of polymer solar cell that uses organic electronics, a branch of electronics that deals with conductive organic polymers or small organic molecules[39], for light absorption and charge transport to produce electricity from sunlight by the photovoltaic effect

f) **Hybrid solar cells**: These cells combine advantages of both organic and inorganic semiconductors. Hybrid photovoltaic has organic materials that consist of conjugated polymers that absorb light as the donor and transport holes [40]. Inorganic materials in hybrid cells are used as the acceptor and electron transporter in the structure. The hybrid photovoltaic devices have a potential for not only low-cost by roll-to-roll processing but also for scalable solar power conversion.

g) **Multijunction solar cell:** Multi-junction (MJ) solar cells are solar cells with multiple p–n junctions made of different semiconductor materials. Each material's p-n junction will produce electric current in response to different wavelengths of light. The use of multiple semiconducting materials allows the absorbance of a broader range of wavelengths, improving the cell's sunlight to electrical energy conversion efficiency.

h) **Quantum Dot solar cell:**A quantum dot solar cell is a solar cell design that uses quantum dots as the absorbing photovoltaic material. It attempts to replace bulk materials such as silicon, copper indium gallium selenide (CIGS) or CdTe. Quantum dots have band gaps that are tunable across a wide range of energy levels by changing the dots' size. In bulk materials the band gap is fixed by the choice of material(s). This property makes quantum dots attractive for multi-junction solar cells, where a variety of materials are used to improve efficiency by harvesting multiple portions of the solar spectrum.

2.3 P-N Junction Solar Cell

A solar cell made of a single p-n junction is called a p-n junction solar cell. It is capable of absorbing photons and converting it to electricity.

2.3.1 Working Principle

Solar cells generate power by utilizing the energy stored in photons of light to create electron-hole pairs in a p-n junction. A solar cell can be thought of as a p-n junction with a resistive load. Even without applied bias, there is an electric field in the depletion region. Photons with a high enough energy create electron-hole pairs in the depletion region that then move, creating a photocurrent I_L in the reverse-bias direction. This current creates a voltage drop across the load, which forward-biases the p-n junction. The forward-bias voltage, in turn, creates a forward-bias current I_F which opposes the photocurrent [41]. The resulting net p-n junction current *I* is

$$I=I_L-I_F \qquad [2.1]$$

The magnitude of the electric field decreases when the junction is forward-biased, but it does not disappear altogether or reverse polarity. The photocurrent is always in the reverse-bias direction, which also causes the net solar cell current to flow in the reverse-bias direction. The p-n junction representation of a solar cell is shown in Figure 2.1.

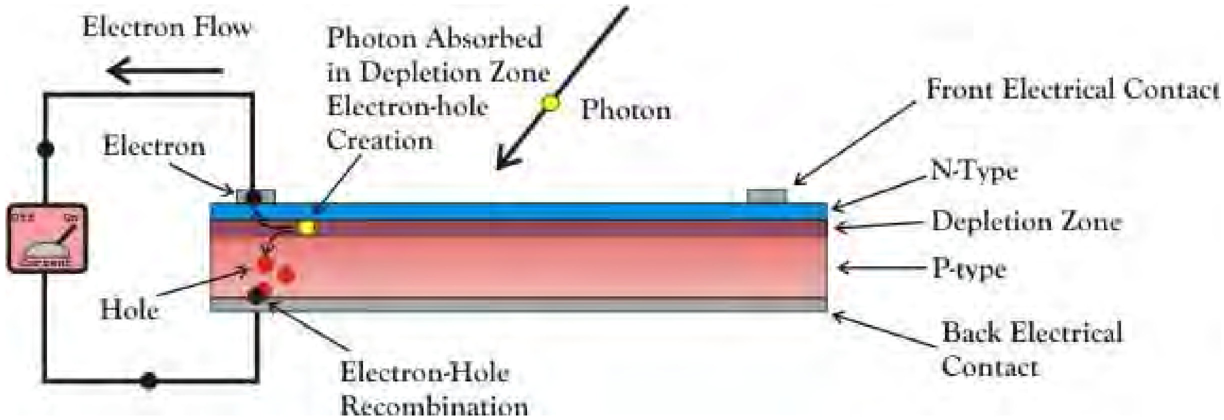

Figure 2.1.P-N junction representation of a solar cell.

2.3.2 Important parameters

The five characteristics that determine the quality of a solar cell are as follows:

a. short circuit current I_{sc},

b. open circuit voltage V_{oc},

c. maximum power P_{max},

d. fill factor FF, and

e. efficiency η

Short circuit current is one of two important limiting parameters of a solar cell. Short circuit current is obtained when the load resistance is zero, causing the voltage to also be zero. The short circuit current is given by

$$I = I_{sc} = I_L \quad [2.2]$$

The other crucial limiting parameter for a solar cell is the **open circuit voltage**. Under the open circuit condition, the load resistance is infinite and the current is zero. The open circuit voltage can then be calculated from

$$V_{oc} = V_t \ln\left(1 + \frac{I_L}{I_S}\right)$$

[2.3]

Here, $I_s$is the reverse saturation current and V_t is the thermal voltage

Each solar cell has a unique I-V curve that begins at zero voltage where the current is I_{SC} and ends where voltage is V_{OC} and current is zero.

A solar cell's **maximum power P_{max}** is an important quality because the purpose of the solar cell is to deliver power to a load. The maximum power rectangle can be found within the I-V curve and is created by drawing straight lines outward from the maximum current and voltage points. An I-V curve for a solar cell with a maximum power rectangle is illustrated in Figure 2. Points A and B in Figure 2 illustrate two possible power rectangles for this solar cell, and the maximum power point MPP shows the maximum power rectangle for this solar cell.

$$P_{max}=V_{max}I_{max}$$

[2.4]

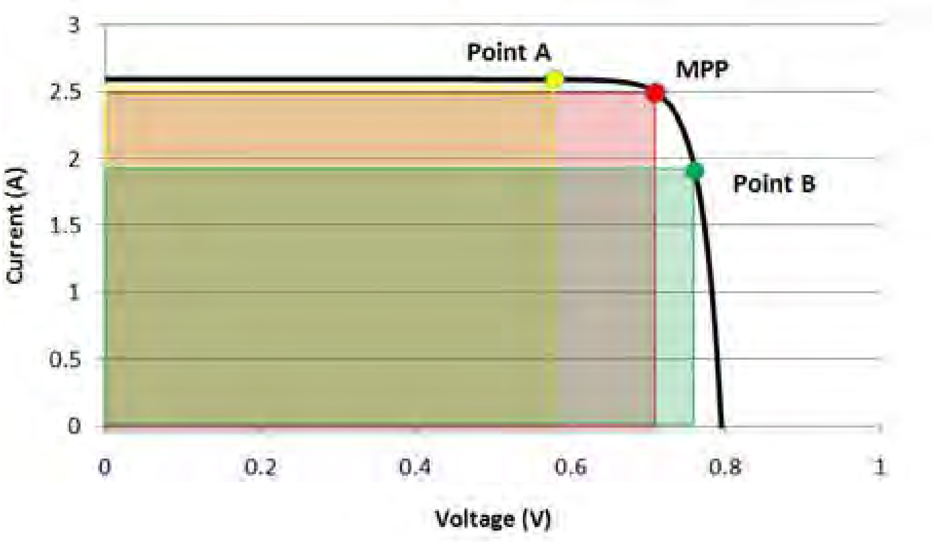

Figure 2.2.I-V curve for a photovoltaic cell showing its maximum power rectangle.

The fill factor FF is a ratio of the maximum power to the power that the open circuit voltage and short circuit current would make if they were multiplied together. The fill factor equation is given by

$$FF = \frac{P_{max}}{V_{oc} I_{sc}}$$

[2.5]

A fill factor of one is ideal because it creates the greatest possible maximum power for the given solar cell. The fill factor can be seen as the sharpness of the “knee” of the I-V curve. If the fill factor is equal to one, the I-V curve is a perfect rectangle.

The last and most important quality of a solar cell is its **efficiency**. A high efficiency cell allows a smaller cell to produce the same amount or more power than a larger cell. A larger cell not only costs more to build but also costs much more to put into space. The calculation for efficiency is given by

$$\eta = \frac{P_{max}}{P_{in}}$$

[2.6]

where P_{in} is the input power from the sun. The parameter P_{in} is based on the air mass number of where the cell is located in relation to the sun. In space, the air mass number (AM0) is zero, meaning all of the energy put out by the sun at that location is receivable because the atmosphere does not intercept and dissipate it as it would on Earth.

. The AM0 spectrum is shown in Figure 2.3.

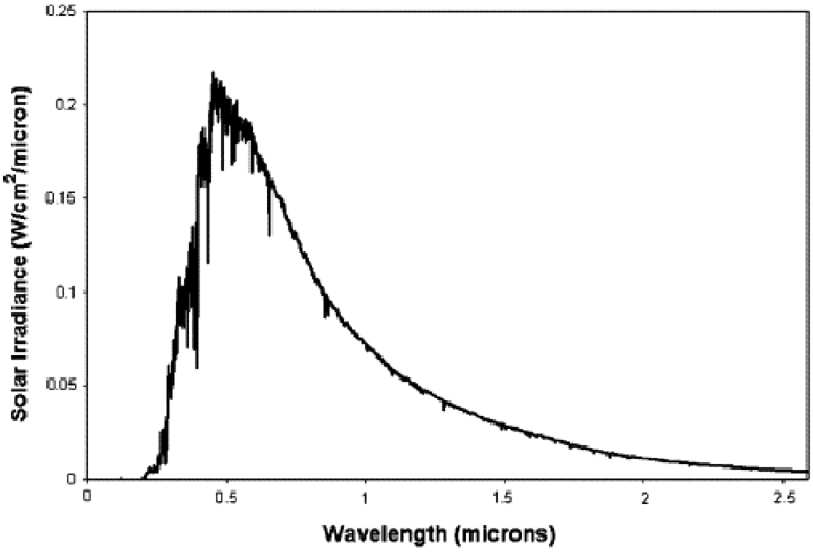

Figure 2.3 AM0 spectrum

2.3.3 Factors affecting solar cell efficiency: There are several factors that affect the solar cell efficiency. The most significant ones are mentioned below.

a) Reflection of photons from the surface of the solar cell: Efficiency is the goal of all solar cell design. There are many factors that lower a solar cell's efficiency, which is why even the best solar cells only output 30 percent of the input power radiated onto them. Any light shone on the surface of a solar cell has the potential to simply reflect off of the surface before it can impart its energy to the electrons in the material. If the angle of incidence is far from perpendicular and the material has a highly reflective surface, then the solar cell can lose as much as 36 percent of the energy. As a solution to this problem, special anti-reflective coatings have been designed, tested, and applied to the surface of the solar cells. At a perpendicular angle of incidence, this coating has been shown to reduce the loss due to reflection by as much as 5 percent.

b) Photons with insufficient energy: The next problem to consider is that all photons have different amounts of energy. The energy needed to cross the band gap is specific to each material. A photon could bombard an electron but not have enough energy to make that electron jump from the valence band to the conduction band. The second issue associated with this fact is that the collision of an under-powered photon with an electron causes it to simply heat up because it cannot cross the band gap. This is not a rare occurrence, and this leads to increased resistance due to the heating of the entire solar cell. Losses due to heating effects also significantly reduce the output.

c) Photons with too much energy: Conversely, photons may carry too much energy. When an over-powered photon collides with an electron, it causes the electron to cross the band gap. The excess energy that was not utilized to cross the band gap is dissipated as heat and causes the same heating effects as the underpowered photon bombardment. Another cause of increased cell temperature is the very phenomenon that allows solar cells to generate current. The electro-static field of the depletion region sweeps charge carriers to opposite sides of the cell and some internal recombination occurs, resulting in heating. The temperature of the cell is crucial to efficient operation. When the cell is above or below its designed operating temperature, the vibration of the crystal lattice structure interferes with the movement of charge carriers through the cell, thus reducing output power.

d) Manufacturing defects: When the semiconductor materials used to make solar cells are manufactured, inevitable defects and impurities are introduced to the finished product. These impurities and defects to the crystal structure cause degraded performance. The metal contacts of the solar cell have an inherent resistance that causes a loss in output power and an increase in the cell’s temperature. These same contacts and the conducting grid on top of the solar cell do not allow light to pass through them and, thus, have a shading effect. This shading effect reduces the input light to the cell by up to 8 percent.

e) Ineffective collisions: Photons are tiny particles, and even though the atoms in a crystal structure are large with respect to a photon, not all photons traveling into a solar cell bombard an electron. Some photons simply enter the cell and pass through without imparting energy. To reduce the effect of this problem, a back surface reflector is added. This reflector doubles the probability that the incoming photon collides with a semiconductor atom because the photon is reflected back through the solar cell after striking the back surface reflector [42].

2.3.4 Loss Mechanisms

The theoretical performance of a solar cell was first studied in depth in the 1960s, and is today known as the Shockley–Queisser limit [3]. The limit describes several loss mechanisms that are inherent to any solar cell design.

The first are the losses due to blackbody radiation, a loss mechanism that affects any material object above absolute zero. In the case of solar cells at standard temperature and pressure, this loss accounts for about 7% of the power. The second is an effect known as "recombination", where the electrons created by the photoelectric effect meet the electron holes left behind by previous excitations. In silicon, this accounts for another 10% of the power. When recombination occurs, a small amount of energy is released and both the electron and the hole disappear.

This energy can be categorized in three ways:

a) Radiative, or the emission of a photon (light), non-radiative, or the emission of a phonon (heat), and Auger, or a transfer of kinetic energy to another free electron or hole. Band-to-band recombination occurs when an electron moves from the conduction band to a hole in the valence band without a change in momentum between the two states. Band-to-band recombinations are typically a radiative transition in direct band gap semiconductors.

b) Surface recombination can have a major impact both on the short-circuit current and on the open-circuit voltage. High recombination rates at the top surface have a particularly detrimental impact on the short-circuit current since top surface also corresponds to the highest generation region of carriers in the solar cell. Lowering the high top surface recombination is typically accomplished by reducing the number of dangling silicon bonds at the top surface by using "passivating" layer on the top surface (Window layer). The majority of the electronics industry relies on the use of a thermally grown silicon dioxide layer to passivate the surface due to the low defect states at the interface. A similar effect is employed at the rear surface to minimize the impact of rear surface recombination velocity on voltage and current if the rear surface is closer than a diffusion length to the junction. A "back surface field" (BSF) [43]-[44] consists of a higher doped region at the rear surface of the solar cell. The interface between the high and low doped region behaves like a *p-n* junction and an electric field forms at the interface which introduces a barrier to minority carrier flow to the rear surface. The minority carrier concentration is thus maintained at higher levels in the bulk of the device and the BSF has a net effect of passivating the rear surface.

c) Trap-assisted recombination begins when an electron gets into a trap, or an energy level within the band gap created by a structural defect or impurity. Eventually, the electron takes a second step and moves back to the valence band and recombines with a hole. This process is also known as Shockley-Read-Hall (SRH) recombination.

d) Auger recombination requires three particles: at least one hole and one electron and the third may be either a hole or an electron. This type of recombination is similar to band-to-band recombination; however, the third particle receives the energy from the recombination. All three of these processes are shown in Figure 1.4.

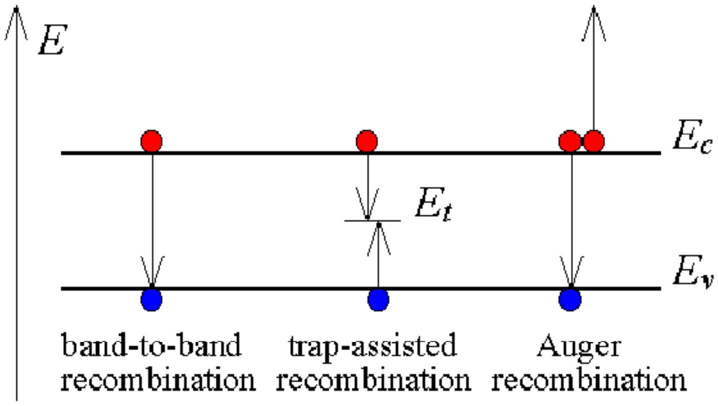

Figure 2.4 Different recombination process

However, the dominant loss mechanism is the inability of a solar cell to extract all of the power in the photon, and the associated problem that it cannot extract any power at all from certain photons. This is due to the fact that the electrons must have enough energy to overcome the band gap of the material.

If the photon has less energy than the band gap, it is not collected at all. This is a major consideration for conventional solar cells, which are not sensitive to most of the infrared spectrum, although that represents almost half of the power coming from the sun. Conversely, photons with more energy than the band gap, say blue light, initially eject an electron to a state high above the band gap, but this extra energy is lost through collisions in a process known as "relaxation". This lost energy turns into heat in the cell, which has the side-effect of further increasing blackbody losses.

Combining all of these factors, the maximum efficiency for a single-band gap material, like conventional silicon cells, is about 34%. That is, 66% of the energy in the sunlight hitting the cell will be lost. Practical concerns further reduce this, notably reflection off the front surface or the metal terminals, with modern high-quality cells at about 22%. Lower, also called narrower, bandgap materials will convert longer wavelength, lower energy photons. Higher, or wider bandgap materials will convert shorter wavelength, higher energy light An analysis of the AM1.5 spectrum, shows the best balance is reached at about 1.1 eV, in the near infrared, which happens to be very close to the natural band gap in silicon and a number of other useful semiconductors.

2. 4 Multijunction solar cell

A conventional single-junction solar cell has a characteristic band gap E_g. When a photon of energy hυ is incident upon the junction, if hυ is greater than E_g, the excess energy is lost as heat within the junction. On the other hand, if hυ is less than E_g, the junction does not absorb the photon and thus captures none of its energy. Of energies from 0 to about 4eV, the efficiency of any single-junction solar cell is inherently limited. A conceptually straightforward way to overcome this limitation is to divide the spectrum into several spectral regions and convert each region with its own junction whose band gap is tuned to that region. Band gap of the materials form the top to the bottom going to be smaller and smaller. It absorbs and converts the photons that have energies greater than the band gap of that layer and less than the band gap of the higher layer [4]-[8]. Availability of materials with optimal band gaps that simultaneously allow high efficiency through low defect densities is the fundamental limitation that multi-junction solar cells suffer from that. Very good candidates to solve the problem and to fabricate such multi-junction cells are alloys of groups III and V. Solar cells made of III-V semiconductor compounds have the potential for high efficiency, their compound materials have advantages including the band gap tunability by elemental compositions, covering a wide range of solar spectrum, higher photon absorption by the direct band gap energies, higher resistivity against high-energy rays in space, and smaller efficiency degradation by heat than Si solar cells. And also by using high-volume growth techniques their complex structures can be grown with extremely high crystalline and optoelectronic quality.

2. 5 The drift diffusion analysis for current

With the use of a relaxation time approximation, the Boltzmann transport equation [45] may be written as:

$$\frac{eE}{m*}\frac{\partial f}{\partial v}+v\frac{\partial f}{\partial x}=\frac{f_0-f(v,x)}{\tau}$$

[2.7]

f= classical distribution function at non equilibrium state that represents the probability of finding a particle at position x. The subscript 0 represents the equilibrium state.

In writing Eq. (2.7) parabolic bands have been assumed for simplicity, and the charge *e* has to be taken with the proper sign of the particle (positive for holes and negative for electrons).

The general definition of current density is given by:

$$J(x)=e\int vf(v,x)dv$$

[2.8]

where the integral on the right hand side represents the first 'moment' of the distribution function. This definition of current can be related to Eq. (2.7) after multiplying both sides of (2.7) by *v* and integrating over *v*. From the RHS of Eq. (2.7) we get

$$\frac{1}{\tau}\left[\int vf_0dv-\int vf(v,x)dv\right]=-\frac{J(x)}{e\tau}$$

[2.9]

The equilibrium distribution function is symmetric in *v*, and hence the first integral is zero. Therefore, we have

$$J(x)=-e\frac{e\tau}{m*}E\int v\frac{\partial f}{\partial v}dv-e\tau\frac{d}{dx}\int v^2f(v,x)dv$$

[2.10]

Integrating by parts we have

$$\int v\frac{\partial f}{\partial v}dv=[vf(v,x)]_{-\infty}^{\infty}-\int f(v,x)dv=-n(x)$$

[2.11]

and we can write

$$\int v^2f(v,x)dv=n(x)\langle v^2\rangle$$

[2.12]

Where $\langle v^2 \rangle$ is the average of the square of the velocity. The drift diffusion equations are derived introducing the mobility $\mu = \frac{e\tau}{m*}$ and replacing $\langle v^2 \rangle$ with its equilibrium value $\frac{k_B T}{m*}$ for a ID case and $\frac{3k_B T}{m*}$ for a 3D case therefore neglecting thermal effects. The diffusion coefficient is also introduced, and the resulting drift diffusion current expressions for electrons and holes are:

$$J_n = qn(x)\mu_n E(x) + qD_n \frac{dn}{dx}$$

$$J_p = qp(x)\mu_p E(x) - qD_p \frac{dn}{dx}$$

[2.14]

respectively where q is used to denote the absolute value of the electronic charge. Although no direct assumptions on the non-equilibrium distribution function, *f*(*v*,*x*), were made in the derivation of Eq. (2.14), in effect, the choice of equilibrium (thermal) velocity means that the drift-diffusion equations are only valid for small perturbations of the equilibrium state (low fields).

The complete drift-diffusion model is based on the following set of equations in 1D:

Current equations

$$J_n = qn(x)\mu_n E(x) + qD_n \frac{dn}{dx}$$

$$J_p = qp(x)\mu_p E(x) - qD_p \frac{dn}{dx}$$

[2.15]

Continuity equations:

$$\frac{\partial n}{\partial t} = \frac{1}{q}\nabla \cdot \mathbf{J_n} + U_n$$

$$\frac{\partial p}{\partial t} = -\frac{1}{q}\nabla \cdot \mathbf{J_p} + U_p$$

[2.16]

Poisson's equation:

$$\nabla \cdot \varepsilon \nabla V = -(p - n + N_D^+ - N_A^-)$$

[2.17]

Where U_n and U_p are the net generation recombination rates.

2. 6 Solution

Two methods can be used, the Gummel’s Iteration Method and the Newton’s Method

2. 6.1 Gummel's Iteration Method

Gummel's method solves the coupled set of semiconductor equations together with the Poisson equation via a decoupled procedure. If we choose the quasi-Fermi level formulation, we solve first a nonlinear Poisson's equation. The potential obtained from this solution is substituted into the continuity equations, which are now linear, and are solved directly to conclude the iteration step. The result in terms of quasi-Fermi levels is then substituted back into Poisson's equation and the process repeated until convergence is reached. In order to check for convergence, one can calculate the residuals obtained by positioning all the terms to the left hand side of the equations and substituting the variables with the iteration values. For the exact solution the residuals should be zero. Convergence is assumed when the residuals are smaller than a set tolerance. The rate of convergence of the Gummel method is faster when there is little coupling between the different equations. The computational cost of one Gummel iteration is one matrix solution for each carrier type plus one iterative solution for the linearization of Poisson's equation. Note that in conditions of equilibrium (zero bias) only the solution of Poisson's equation is necessary, since the equilibrium Fermi level is constant and coincides with both quasi-Fermi levels. We give some examples of the quasi-linearization of Poisson equation, as necessary when Gummel's method is implemented. Let us consider the 1-D case in equilibrium first. As mentioned earlier, one has to solve only Poisson's equation, since the current is zero and the exact expressions for the carrier concentrations are known. In the non-degenerate case, the explicit expressions for the electron and hole densities are substituted into Poisson's equation to give

$$\frac{d^2V}{dx^2} = \frac{q}{\varepsilon}\left[n_i \exp(-q\emptyset_n)\exp\left(\frac{qV}{k_BT}\right) - n_i \exp\left(q\emptyset_p\right)\exp\left(-\frac{qV}{k_BT}\right) + N_A - N_D\right]$$

[2.18]

which is sometimes referred to as the non-linear Poisson equation due to the nonlinear terms involving V on the RHS. In equilibrium, the quasi-Fermi energies are equal and spatially invariant, hence we may choose the Fermi energy as the reference energy, i.e. $\emptyset_p = \emptyset_n = 0$

Furthermore, the equation may be scaled by using the (minimum) extrinsic Debye length for the space coordinate x, and the thermal voltage $\frac{k_B T}{q}$ for the potential V. Writing $\bar{V}$ and $\bar{x}$ for the normalized potential and space coordinates, we obtain

$$\frac{d^2\bar{V}}{d\bar{x}^2} = \frac{n_i}{N}\left[\exp(\bar{V}) - \exp(-\bar{V}) + \frac{N_A - N_D}{n_i}\right]$$

[2.19]

The equilibrium non-linear Poisson equation can be solved with the following quasi-linearization procedure

1. Choose an initial guess for the potential V .

2. Write the potential at the next iteration step as Vnew = + V δV , and substitute into Eq. (2) to solve for Vnew to give

$$\frac{d^2\bar{V}}{d\bar{x}^2} + \frac{d^2\delta V}{d\bar{x}^2} = \frac{n_i}{N}\left[\exp(\bar{V})\exp(\delta V) - \exp(-\bar{V})\exp(-\delta V) + \frac{N_A - N_D}{n_i}\right]$$

[2.20]

3.Use the linearization $\exp(\pm\delta V) \approx 1 + \delta V$and discretize the resultant equation. This equation has a tridiagonal matrix form and is readily solved for $\delta V(i)$

$$\begin{aligned} \delta V(i-1) - \left[2 + \frac{n_i}{N}\Delta^2 x\left[exp\left(\bar{V}(i)\right) - exp\left(-\bar{V}(i)\right)\right]\right]\delta V(i) + \delta V(i+1) \\ = -\bar{V}(i-1) + 2\bar{V}(i) - \bar{V}(i+1) \\ + \frac{n_i}{N}\Delta^2 x\left[exp\left(\bar{V}(i)\right) - exp\left(-\bar{V}(i)\right) + \frac{N_A - N_D}{n_i}\right] \end{aligned}$$

[2.21]

4. Check for convergence. The residual of equation (2.21) is calculated and convergence is achieved if the norm of the residual is smaller than a preset tolerance. If

the convergence is not achieved return to step 2.In practice one might simply check the norm of the error

$$\|\delta V\|_2 \leq Tol\text{or}\|\delta V\|_\infty \leq Tol$$

[2.22]

Note that for the solution of the nonlinear Poisson's equation, the boundary conditions are referenced to the equilibrium Fermi level. One may use the separation between the Fermi level and the intrinsic Fermi level at the contacts for the boundary conditions.

After the solution in equilibrium is obtained, the applied voltage is increased gradually in steps $\Delta V \leq k_B T/q$ to avoid numerical instability. The scaled nonlinear Poisson equation under nonequilibrium conditions now becomes

$$\frac{d^2V}{dx^2} = \frac{n_i}{N}\left[\exp(-\emptyset_n)\exp(V) - \exp\left(-\emptyset_p\right)\exp(-V) + \frac{N_A - N_D}{n_i}\right]$$

[2.23]

where the quasi-Fermi levels are also normalized. Assuming Einstein’s relations still hold, the current density equation may be re-written as

$$\begin{aligned} J_n &= -q\mu_n n\frac{\delta V}{\delta x} + q\mu_n\frac{k_B T}{q}\frac{\partial}{\partial x}\left[n_i exp\left(\frac{q(V-\emptyset_n)}{k_B T}\right)\right] \\ &= -q\mu_n n\frac{\delta V}{\delta x} + q\mu_n\frac{k_B T}{q}n\frac{q}{k_B T}\left[\frac{\partial V}{\partial x} - \frac{\partial\emptyset_n}{\partial x}\right] \\ &= -q\mu_n n\frac{\delta\emptyset_n}{\delta x} \\ &= -q\mu_n n_i exp\left(\frac{q(V-\emptyset_n)}{k_B T}\right)\frac{\delta\emptyset_n}{\delta x} \\ &= -q\mu_n n_i exp\left(\frac{qV}{k_B T}\right)\frac{-k_B T}{q}\frac{\partial}{\partial x}exp\left(\frac{-q\emptyset_n}{k_B T}\right) \end{aligned}$$

[2.24]

which may be written more compactly, including quasi-Fermi level normalization, as

$$J_n = a_n(x)\frac{\delta}{\delta x}exp(-\emptyset_n)$$

[2.25]

A similar formula is obtained for the holes

$$J_p = a_p(x)\frac{\delta}{\delta x}exp\left(\emptyset_p\right)$$

[2.26]

and the continuity equations are therefore given by

$$\frac{\delta}{\delta x}\left[a_n(x)\frac{\delta}{\delta x}exp(-\emptyset_n)\right] = qU(x)$$

[2.27]

$$\frac{\delta}{\delta x}\left[a_p(x)\frac{\delta}{\delta x}exp\left(-\emptyset_p\right)\right] = qU(x)$$

[2.28]

The continuity equations may be discretized with a straightforward finite difference approach (here for simplicity with uniform mesh)

$$\frac{\frac{a_a\left(i+\frac{1}{2}\right)[\Phi_a(i+1)-\Phi_a(i)]}{\Delta x}-\frac{a_a\left(i-\frac{1}{2}\right)[\Phi_a(i)-\Phi_a(i-1)]}{\Delta x}}{\Delta x} = U$$

[2.29]

where the Slotboom variables have been used for simplicity of notation. Note that the inner derivative has been discretized with centered differences around the points $(i \pm 1/2)$ of the interleaved mesh. Variables on the interleaved mesh must be determined very carefully, using consistent interpolation schemes for potential and carrier density, as discussed later. The discretized continuity equations lead to the tridiagonal system

$$a_n\left(i-\frac{1}{2}\right)\Phi_n(i-1)-\left[a_n\left(i+\frac{1}{2}\right)+a_n\left(i-\frac{1}{2}\right)\right]\Phi_n(i)+a_n\left(i+\frac{1}{2}\right)\Phi_n(i+1) = \Delta^2 xU(i)$$

[2.30]

$$a_p\left(i-\frac{1}{2}\right)\Phi_p(i-1)-\left[a_p\left(i+\frac{1}{2}\right)+a_p\left(i-\frac{1}{2}\right)\right]\Phi_p(i)+a_p\left(i+\frac{1}{2}\right)\Phi_p(i+1)$$
$$=-\Delta^2xU(i)$$

[2.31]

The decoupled iteration now solves Poisson's equation, initially with a guess for the quasi-Fermi levels. The voltage distribution obtained for the previous voltage considered is normally a good initial guess for the potential. Since the quasi-Fermi levels are inputs for Poisson's equation, the quasi-linearization procedure for equilibrium can be used again. The potential is then used to update the $a_n(i)$ and$a_p(i)$ Eqs. (2.30) and (2.31) are solved to provide new quasi-Fermi level values for Poisson's equation, and the process is repeated until convergence is reached. The generation-recombination term depends on the electron and hole concentrations, therefore it has to be updated at each iteration. It is possible to update the generation-recombination term also intermediately, using the result for the electron concentration. The examples given bellow illustrates the Gummel's approach that is limited to the non-degenerate case. If field dependent mobility and diffusion coefficients are introduced, minimal changes should be necessary, as long as it is still justified the use of Einstein's relations. Extension to non uniform mesh is left as an exercise for the reader. In the 2-D case, the quasi-linearized Poisson's equation becomes

$$-\left(4+h^2\frac{n_i}{N}\left[\Phi_n(i,j)\exp\big(V(i,j)\big)+\Phi_p(i,j)\exp\big(-V(i,j)\big)\right]\right)\partial V(i,j)$$
$$+\left[\partial V(i-1,j)+\partial V(i+1,j)+\partial V(i,j-1)+\partial V(i,j+1)\right]$$
$$=4V(i,j)-V(i-1,j)-V(i+1,j)-V(i,j-1)-V(i,j+1)$$
$$+h^2\frac{n_i}{N}\left[\Phi_n(i,j)\exp\big(V(i,j)\big)+\Phi_p(i,j)\exp\big(-V(i,j)\big)+\frac{N_A+N_B}{n_i}\right]$$

[2.32]

The normalized mesh size is h=Δx=Δy. As before the thermal voltage k_BT/q has been used to normalize the potential V and the quazi-Fermi levels ϕ_n and ϕ_p included in the slotboom variables $\Phi_{n,p}$=exp(±$\phi_{n,p}$)

The continuity equations with the form $\nabla\cdot(a(x,y)\nabla\Phi)=\pm U(x,y)$ are discretized as

$$
\begin{aligned}
-\left[a\left(i+\frac{1}{2},j\right)+a\left(i-\frac{1}{2},j\right)+a\left(i,j+\frac{1}{2}\right)+a\left(i,j-\frac{1}{2}\right)\right]\Phi(i,j) \\
+a\left(i+\frac{1}{2},j\right)\Phi(i+1,j)+a\left(i-\frac{1}{2},j\right)\Phi(i-1,j) \\
+a\left(i,j+\frac{1}{2}\right)\Phi(i,j+1)+a\left(i,j-\frac{1}{2}\right)\Phi(i,j-1)=\pm h^2U(i,j)
\end{aligned}
$$

[2.33]

2. 6.2 Newton's Method

Newton's method is a coupled procedure which solves the equations simultaneously, through a generalization of the Newton-Raphson method for determining the roots of an equation.

We rewrite Eqs. (2.23, 2.27, 2.28) in the residual form

$W_V(V,n,p)=0$ $W_n(V,n,p)=0$ $W_p(V,n,p)=0$

[2.34]

Starting from an initial guess V_o , n_o , and p_o , the corrections V, Δn , and Δp are calculated from the Jacobian system

$$
\begin{bmatrix}
\frac{\delta W_V}{\delta V} & \frac{\delta W_V}{\delta n} & \frac{\delta W_V}{\delta p} \\
\frac{\delta W_n}{\delta V} & \frac{\delta W_n}{\delta n} & \frac{\delta W_n}{\delta p} \\
\frac{\delta W_p}{\delta V} & \frac{\delta W_p}{\delta n} & \frac{\delta W_p}{\delta p}
\end{bmatrix}
\begin{pmatrix} \Delta V \\ \Delta n \\ \Delta p \end{pmatrix}
= -\begin{pmatrix} W_V \\ W_n \\ W_p \end{pmatrix}
$$

[2.35]

which is obtained by Taylor expansion. The solutions are then updated according to the scheme

$$V(k+1)= V(k)+\Delta V(k)$$

$$n(k+1) = n(k) + \Delta n(k)$$

$$p(k+1) = p(k) + \Delta p(k)$$

[2.36]

where k indicates the iteration number. In practice, a relaxation approach is also applied to avoid excessive variations of the solutions at each iteration step. The system (2.35) has 3 equations for each mesh point on the grid. This indicates the main disadvantage of a full Newton iteration, related to the computational cost of matrix inversion (one may estimate that a 3N× N matrix takes typically 20 times longer to invert than an analogous N ×N matrix). On the other hand convergence is usually fast for the Newton method, provided that the initial condition is reasonably close to the solution, and is in the neighborhood where the solution is unique. There are several viable approaches to alleviate the computational requirements of the Newton's method. In the Newton-Richardson approach, the Jacobian matrix is updated only when the norm of the error does not decrease according to a preset criterion. In general, the Jacobian matrix is not symmetric positive definite, and fairly expensive solvers are necessary. Iterative schemes have been proposed to solve each step of Newton's method by reformulating Eq. (2.35) as

$$\begin{bmatrix} \frac{\delta W_V}{\delta V} & 0 & 0 \\ \frac{\delta W_n}{\delta V} & \frac{\delta W_n}{\delta n} & 0 \\ \frac{\delta W_p}{\delta V} & \frac{\delta W_p}{\delta n} & \frac{\delta W_p}{\delta p} \end{bmatrix} \begin{pmatrix} \Delta V \\ \Delta n \\ \Delta p \end{pmatrix}_{k+1} = -\begin{pmatrix} W_V \\ W_n \\ W_p \end{pmatrix} - \begin{bmatrix} 0 & \frac{\delta W_V}{\delta n} & \frac{\delta W_V}{\delta p} \\ 0 & 0 & \frac{\delta W_n}{\delta p} \\ 0 & 0 & 0 \end{bmatrix} \begin{pmatrix} \Delta V \\ \Delta n \\ \Delta p \end{pmatrix}_{k}$$

(2.37)

Since the matrix on the left hand side is lower triangular, one may solve Eq. (2.37) by decoupling into three systems of equations solved in sequence. First, one solves the block of equations (again, one for each grid point)

$$\frac{\delta W_V}{\delta V}(\Delta V)_{k+1} = -W_V - \frac{\delta W_V}{\delta n}(\Delta n)_k - \frac{\delta W_V}{\delta p}(\Delta p)_k$$

[2.38]

And the result is used in the next block of equations

$$\frac{\delta W_n}{\delta n}(\Delta n)_{k+1} = -W_n - \frac{\delta W_n}{\delta V}(\Delta V)_{k+1} - \frac{\delta W_n}{\delta p}(\Delta p)_k$$

[2.39]

Similarly for the third block

$$\frac{\delta W_p}{\delta p}(\Delta p)_{k+1} = -W_p - \frac{\delta W_p}{\delta V}(\Delta V)_{k+1} - \frac{\delta W_p}{\delta n}(\Delta n)_{k+1}$$

[2.40]

The procedure achieves a decoupling of the equations as in a block Gauss-Seidel iteration, and can be intended as a generalization of the Gummel method. A block-SOR method is obtained if the left hand sides are pre-multiplied by a relaxation parameter. This iteration procedure has better performance if the actual variables are (V, φ_n, φ_p). In general, Gummel's method is preferred at low bias because of its faster convergence and low cost per iteration. At medium and high bias the Newton's method becomes more convenient, since the convergence rate of Gummel's method becomes worse as the coupling between equations becomes stronger at higher bias. But since Gummel's method has a fast initial error reduction, it is often convenient to couple the two procedures, using Newton's method after several Gummel's iterations. Remember that it is very important for the Newton's iteration to start as close as possible to the true solution. Close to convergence, the residual in Newton's iteration should decrease quadratically from one iteration to the other.

Generation and Recombination

The Shockley-Reed-Hall model is very often used for the generation-recombination term due to trap levels

$$U_{SRH} = \frac{np - n_i^2}{\tau_p \left[n + n_i exp\left(\frac{q(E_t - E_i)}{k_B T}\right)\right] + \tau_n \left[p + n_i exp\left(\frac{q(E_i - E_t)}{k_B T}\right)\right]}$$

[2.41]

Where E_t is the trap energy level involved and τ_n and τ_p are the electron and hole lifetimes. Surface rates may be included with a similar formula in which the lifetimes are substituted by $\frac{1}{S_{n,p}}$ where $S_{n,p}$ is the surface recombination velocity

The Auger recombination may be accounted for by using the formula

$$U_{AUG} = C_n[pn^2 - nn_i^2] + C_p[np^2 - pn_i^2]$$

[2.42]

whereC_n and C_p are appropriate constants. The Auger effect is for instance very relevant in the modeling of highly doped emitter regions in bipolar transistors. The generation process due to impact ionization can be included using the field dependent rate

$$U_I = \frac{a_n^{\infty} exp\left(\frac{-E_n^{crit}}{E}\right)^{\beta n} |J_n| + a_p^{\infty} exp\left(\frac{-E_p^{crit}}{E}\right)^{\beta p} |J_p|}{q}$$

[2.43]

2.7 Simulation Software

2.7.1 SILVACO

Silicon Valley Company (Silvaco) is a leading vendor in technology computer aided design (TCAD). Established in 1984 and located in Santa Clara, California, Silvaco has developed a number of exceptional CAD simulation tools to aid in semiconductor process and device simulation.

2.7.2 ATLAS© /DECKBUILD

The ability to accurately simulate a semiconductor device is critical to industry and research environments. The ATLAS© device simulator is specifically designed for 2D and 3D modeling to include electrical, optical and thermal properties within a semiconductor device[46]. ATLAS© provides an integrated physics-based platform to analyze DC, AC and time-domain responses for all semiconductor-based technologies. The powerful input syntax allows the user to design any semiconductor device using both standard and user-defined material of any size and dimension. ATLAS© also offers a number of useful device examples to assist in your own unique design.

DeckBuild is the run time environment used to input a command file or deck and is given the extension ".in". To run ATLAS© in the DeckBuild environment, the user must first call the ATLAS© simulator with the command:

```
go atlas
```

This chapter gives a brief description of how Atlas works. The main order andframework for building code is shown in the following table.

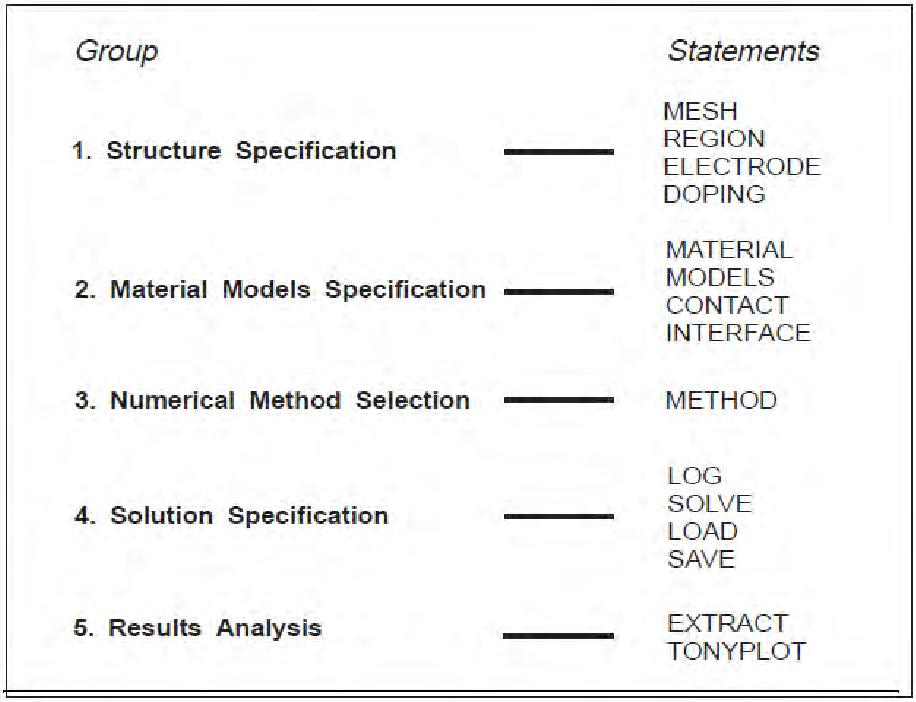

Group	*Statements*
1. Structure Specification	MESH REGION ELECTRODE DOPING
2. Material Models Specification	MATERIAL MODELS CONTACT INTERFACE
3. Numerical Method Selection	METHOD
4. Solution Specification	LOG SOLVE LOAD SAVE
5. Results Analysis	EXTRACT TONYPLOT

Table 2.1 Command Groups and Statements [46]

The order of command in this table must be followed. Failure to comply may lead not only to the termination of the program, but to incorrect operation and faulty results.

2.7.3 ATLAS General Device Construction Outline

1. Mesh

The first step in building a device after the go atlas statement is to define the mesh. The mesh is a grid that covers the physical area in which the device will be constructed and simulated. The mesh is simply created by a series of vertical and horizontal lines with user defined spacing between them [47].

The mesh is created with the following statements:

```
MESH SPACE.MULT=<VALUE>;

X.MESH LOCATION=<VALUE> SPACING=<VALUE>;

Y.MESH LOCATION=<VALUE> SPACING=<VALUE>.
```

The first line of code specifies a scaling factor for the mesh that is created by the X.MESH and Y.MESH commands.

The default value is one but can be changed to generate a finer mesh by substituting a value less than one or a courser mesh by substituting a value greater than one [42]. The benefit of a courser mesh is a faster simulation speed but at the cost of a less accurate model. The opposite is true for a finer mesh.

The next two lines contain the commands X.MESH and Y.MESH. They are used to specify the locations of the mesh vertical and horizontal lines in microns using the spacing defined in that line. In order for these commands to work, X.MESH and Y.MESH statements must be listed in the order of increasing *x* and *y*. Also, both negative and positive values of *x* and *y* are allowed [47]. An example of fine and course meshes created in ATLAS is illustrated in Figure 2.5

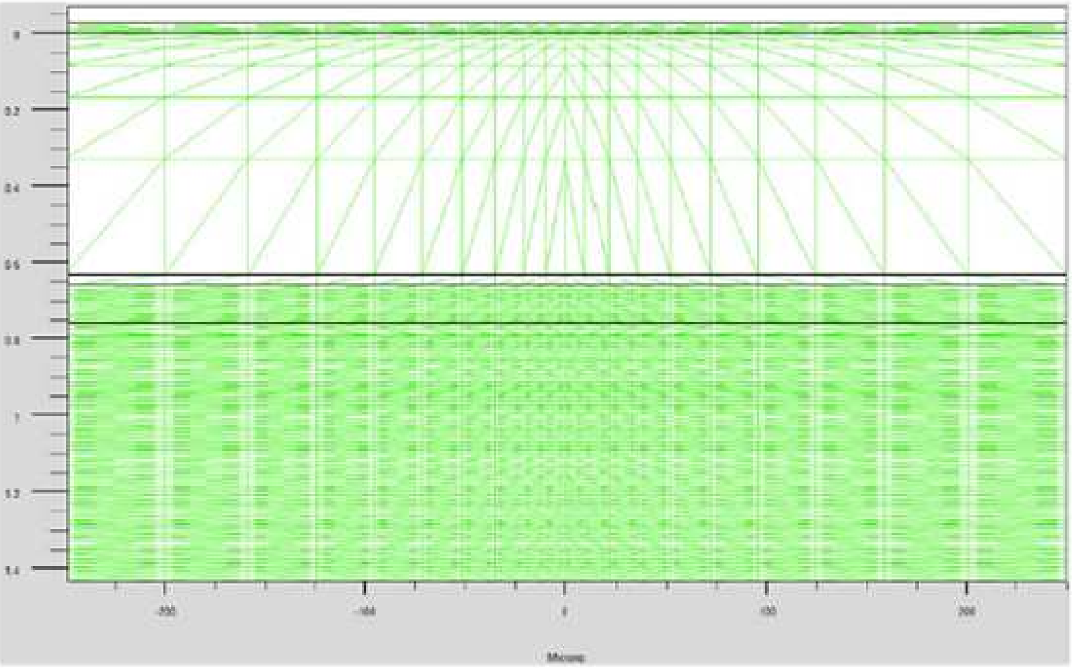

Figure 2.5 Fine and coarse mesh in ATLAS

2. Regions

The next step in creating a semiconductor device is to separate the created mesh into regions. The format to define the regions is:

REGION number=<integer><material_type> /
<position parameters>.

This statement can be broken up into several parts. First, the selected integer creates a region that can be referred to by that same integer. The material type determines what element or compound this region becomes and must be available in the ATLAS database.

Last, the position parameters tell ATLAS which potion of the mesh that was just created will become the region. The position parameters must be contained within the bounds of the mesh that was created in the first step [42]. An example of created regions can be found in Figure 2.6.

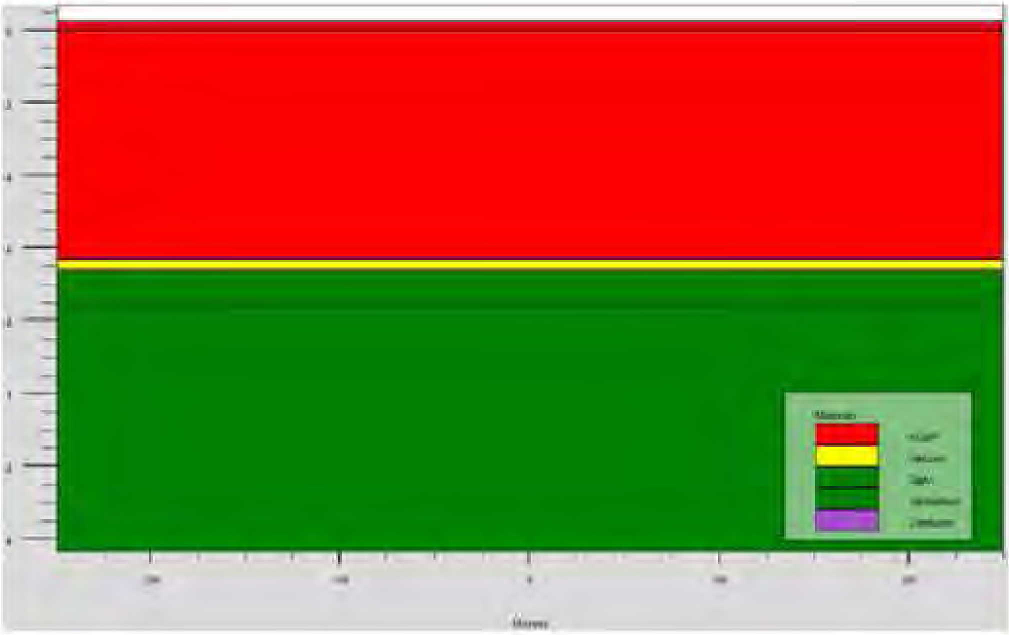

Figure 2.6 Regions created in a semiconductor device

3. Electrode

Once the regions are set, the electrodes must be assigned to the desired region so that it can be electrically analyzed. The electrode can be assigned to any region or portion of a region including the “top” or “bottom” as it is in this research. Because this tunnel junction is intended to be used as an interconnect between two solar cells, it was unnecessary to assign the electrodes to metal contacts or large areas that would constitute superfluous calculations or error. Therefore, the anode was assigned to the top of the junction and cathode was assigned to the bottom. The following statements were used to define these parameters:

```
#electrodes
electrode name=anode top
electrode name=cathode bottom
```

4. Doping

The last required input of the structure specification is the doping statement. The doping statement is used to assign the doping level within the previously assigned regions. Various properties can be appended to the doping statement to specify how the semiconductor was doped and of whether the region is n- or p-type. The desired I-V relationship in forward bias will determine the doping characteristics of the semiconductor. However, the following statements were developed for a Si junction with a forward bias current of approximately 12A at 0.06V:

```
doping uniform p.typeconc=5e19 y.max=0.5
doping uniform n.typeconc=1e20 y.min=0.5
```

Here the regions were already defined in a previous statement and were therefore referred to by their region number. Region 1 was uniformly doped with a p-type material with a concentration of 5e19. Similarly, region 2 was uniformly doped with an n-type material at a concentration of 1e20.

2.7.4 Material Models Specification

1. Material

The material statement relates physical parameters with the materials assigned to the mesh. The important material parameters for most standard semiconductors are already defined by ATLAS© and therefore do not require any changes. We utilized the extensive model libraries in ATLAS© since the developed tunnel junctions were based in Si, Ge, and GaAs which are all very well researched and documented.

2. Models

The models statement is essential to the accurate modeling of a particular phenomenon because it sets flags for ATLAS© to indicate the inclusion of different mathematical models, physical mechanisms and other global parameters such as substrate temperature. The model statement and parameters used in this research are listed below:

```
models temperature=300 srh Fermi ni.fermi print qtunn.dir=0 \
bbt.nonlocal bbt.forward bbt.nlderivs
```

As with all ATLAS© statements, a complete list of modeling parameters and their definitions can be found in the ATLAS© User's Manual [11]. The most notable parameters for the calculation of the quantum tunneling effect are qtunn.dir, bbt.nonlocal, bbt.forward and bbt.nlderivs. qtunn.dir specifies the direction of tunneling across the junction. Since this device was set up for tunneling across the y-axis, the parameter value was set to zero (to specify tunneling in x-direction, qtunn.dir = 1). The bbt.nonlocal, bbt.forward and bbt.nlderivs parameters enable the non-local band-to-band tunneling model to be used in forward bias and allow the use of the non-local derivatives in the Jacobian matrix which helps eliminate convergence problems.

3. Contact

Since the tunnel junction is meant to be used as an interconnect of a single crystal multi-junction solar cell there was no need to specify any contact parameters. The electrode statements assigning the cathode and anode to the semiconductor were sufficient for calculating the current through the junction.

2.7.5 Numerical Method Selection

The method statement specifies the numerical methods to be used in the calculations specified in the model statement. The quantum tunneling through a junction is highly dependent on the carrier concentration. Therefore, it is very important to accurately measure the carrier concentration for each iteration. This is done by defining the climit parameter in the method statement, which specifies the normalization factor to limit the step size of the potential update. The parameter dvmax sets the maximum allowed potential updates per iteration. Reducing dvmax dampens the oscillations in the small I-V calculations.

2.7.6 Solution Specification

The log/solve/save statements are used to create data files in ATLAS© simulations. These statements work together to be provide data to be analyzed by other functions. This research I have used these three statements as a tool to check bias points, energy band diagrams and carrier concentrations as a result of varying stimuli.

1. Log

The log statement allows all terminal characteristics generated by a solve statement to be saved to a file.

2. Solve

The solve statement specifies which bias points are to be applied to produce an output. The bias points can be set in a number of different way including step, initial and lambda depending on what stimulus is desired.

3. Save

The save statement is used to save all node point data into an output file. A common use of the log/solve/save statements for the tunnel junction studied is shown below:

```
log outfile=tjsi.log
```

```
solve name=anode vanode =-1 vstep=0.1 vfinal=0.0
solve name=anode vanode =0.0 vstep=0.01 vfinal=0.2
solve name=anode vanode =0.2 vstep=0.1 vfinal=1.5
save outfile=tjsi.log
```

Here the output file tjsi.log has been set aside to store data from the solve statements and then saved so that the data can be called at a later time. The solve statements simply sweep the voltage from -1V to 1.5V in varying voltage steps depending on the degree of accuracy at the desired range. With the date stored in an outfile, it is ready to be displayed so that it can be analyzed.

Chapter 3

RESULTS AND DISCUSSIONS

3.1 Introduction

In this chapter a complete simulation of an InGap/GaAs/Si_xGe_{1-x}solar cell is performed. The three subcells are analyzed individually and then together in a mechanically stacked configuration. Also, the bottom cell material composition is varied and several parameters are optimized. Key values are extracted from the plots which helped us decide the optimum configuration of a highest efficiency solar cell.

3.2 Solar Cell Structure

InGaP (Eg=1.9eV) is used as the top cell material for our solar cell. Next, A very common material is used for the middle cell, GaAs (Eg=1.42eV). The bottom cell is made of Si_xGe_{1-x} compound semiconductor, and in this work, its composition is varied and cell performance is observed. We start off with a bottom cell configuration of $Si_{0.11}Ge_{0.89}$ and subsequently investigated for $Si_{0.20}Ge_{0.80}$, $Si_{0.28}Ge_{0.72}$, $Si_{0.65}Ge_{0.35}$, $Si_{0.85}Ge_{0.15}$ and $Si_{0.98}Ge_{0.02}$ also.

Additionally a heavily doped AlInGaP material is used as a BSF layer, which helps reduce carrier scattering [43]-[44]. However, the junction of the subsequent layer and the BSF should not create a field that opposes the movement of carriers towards the electrodes. For this reason, a heavily doped GaAs buffer layer is grown between them. For purposes of mechanical strength, the cell should also be built on a much thicker substrate, Si_xGe_{1-x} in this case. A window layer of AlInP material is added to reduce surface recombination. Finally a Si_3N_4 ARC layer is added on top to minimize reflections. A cap layer and real golden contacts are also added. The bottom contact is shined and becomes a back surface reflector (BSR) to reflect photons back into the cell. For simplicity, at this step, the electrodes are considered to be ideal and transparent.

The complete structure can be drawn as follows:

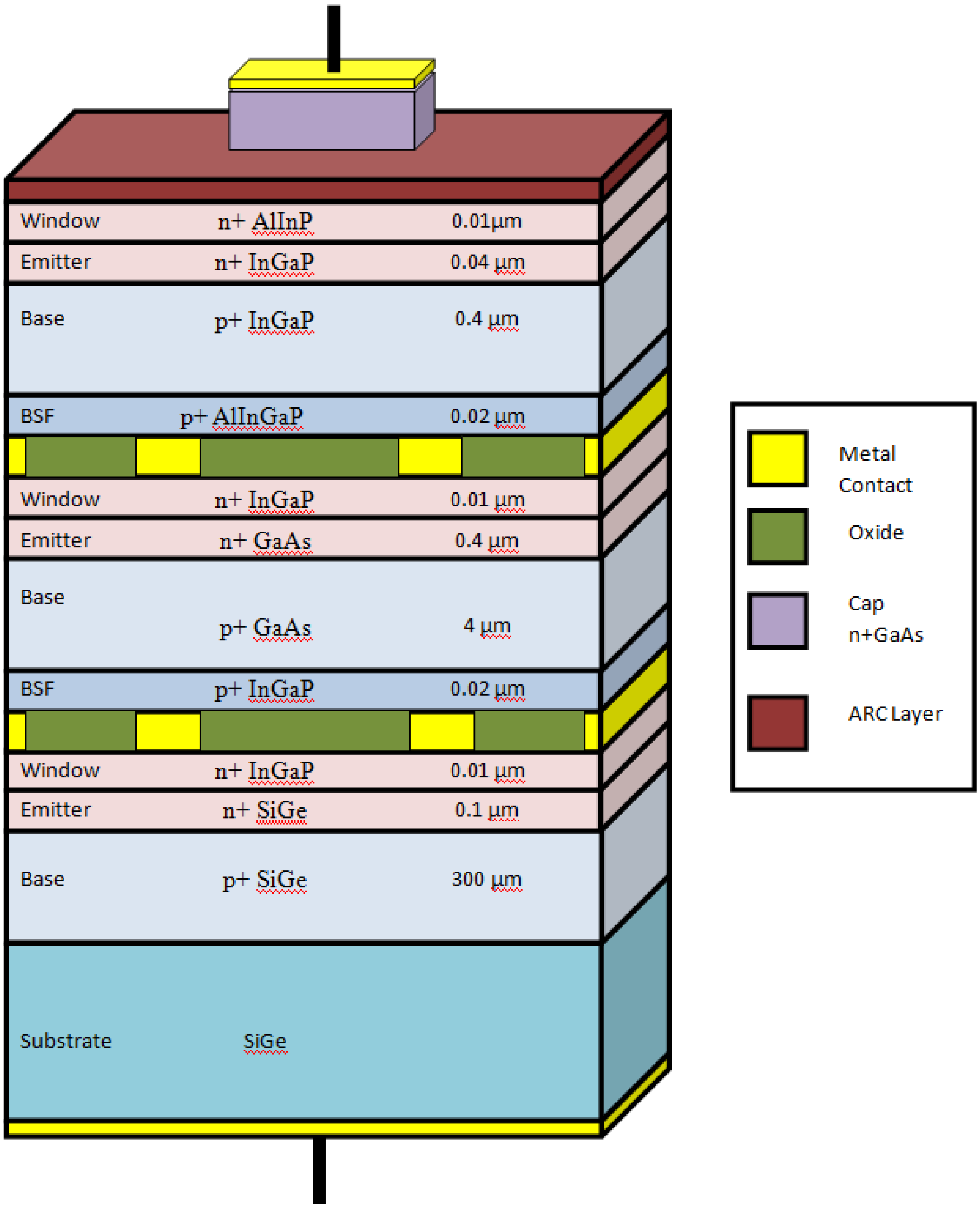

Figure 3.1 Complete solar cell structure

3.3 I-V Characteristics

The I-V characteristics of the individual subcells are first shown in Fig 3.2- Fig 3.4 and then the overall I-V characteristic is shown for the Multijunction solar cell, with bottom cell composition of $Si_{0.11}Ge_{0.89}$ in Fig 3.5. I–V characteristic is used to determine the cell's operating point, fill factor and efficiency which are shown in Table 1.

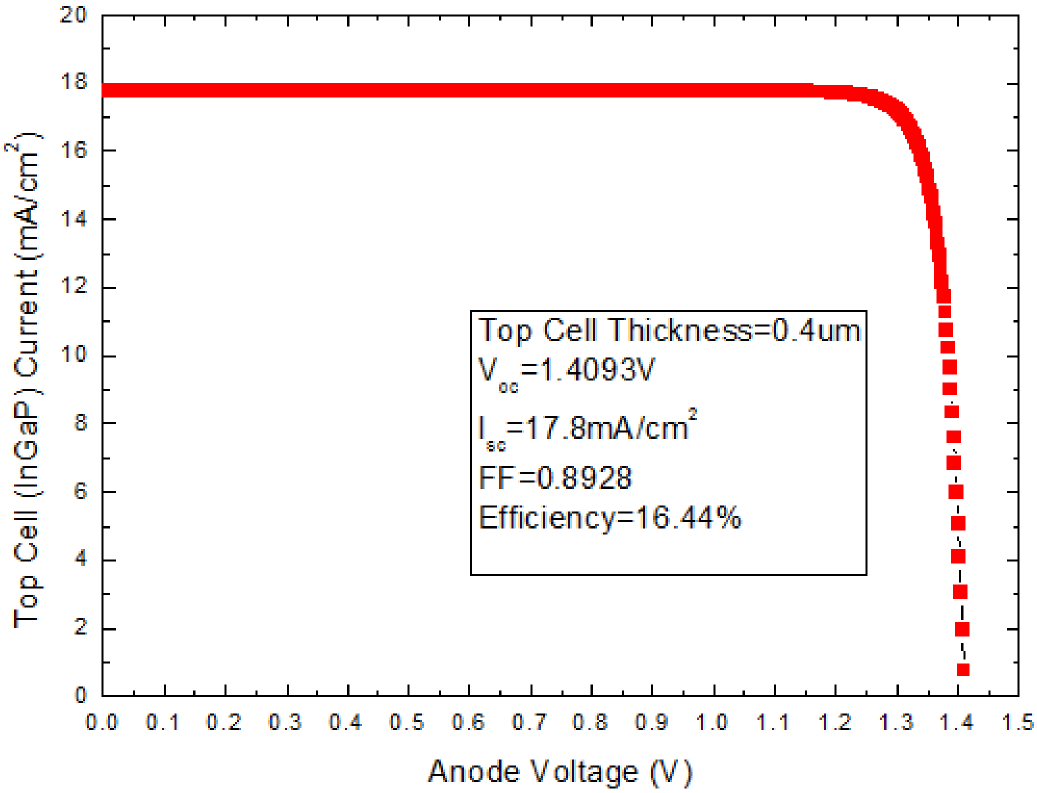

Figure 3.2 I-V characteristic of InGaP top cell.

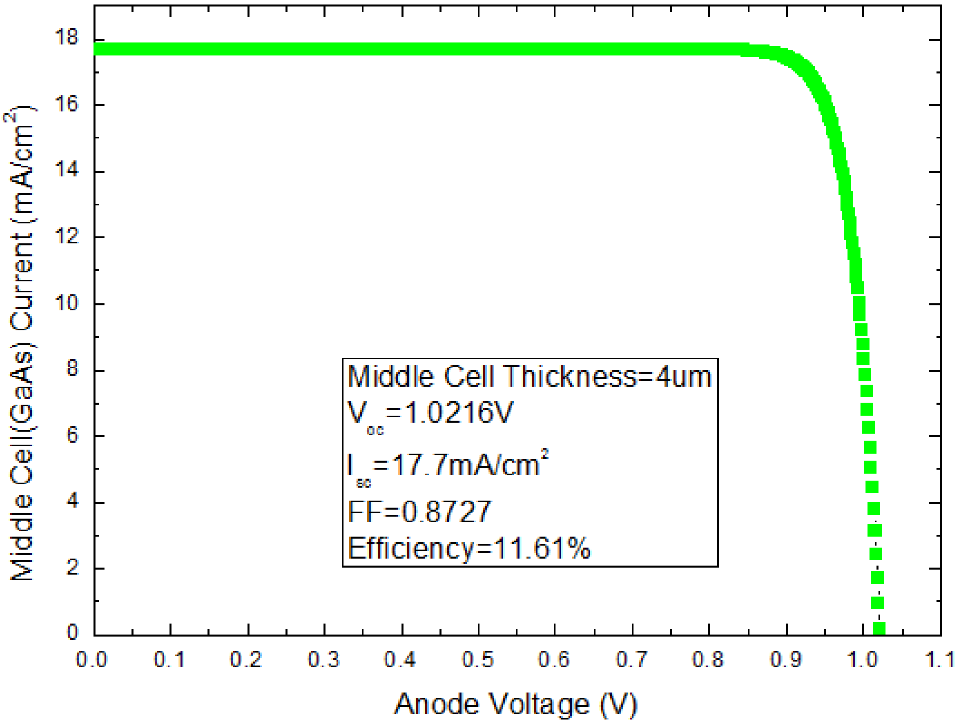

Figure 3.3 I-V characteristic of GaAs middle cell

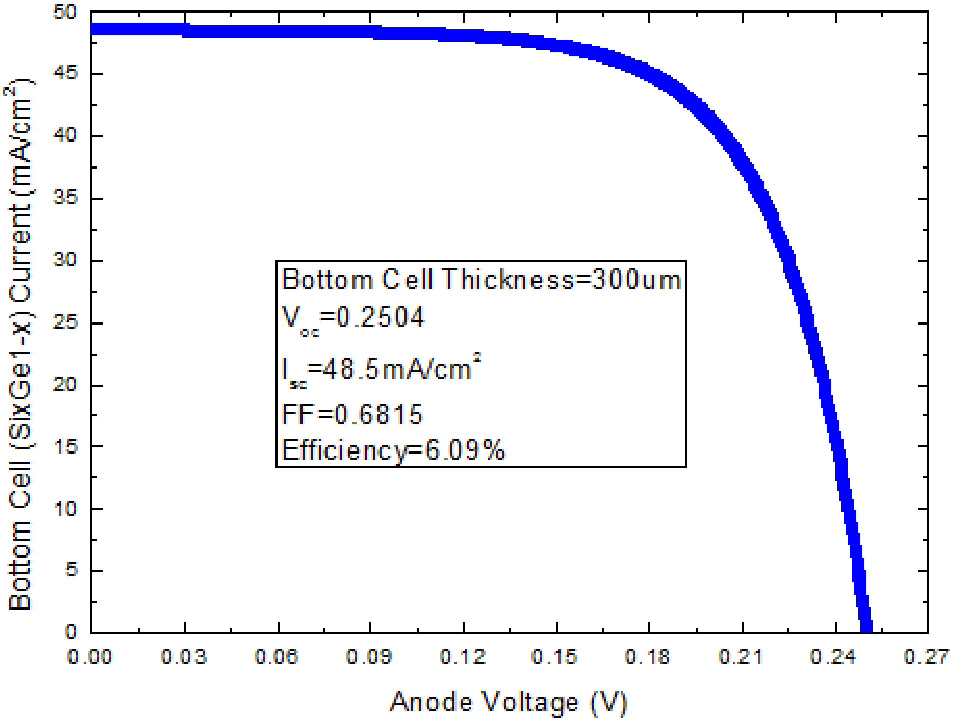

Figure 3.4 I-V characteristic of $Si_{11}Ge_{89}$ bottom cell

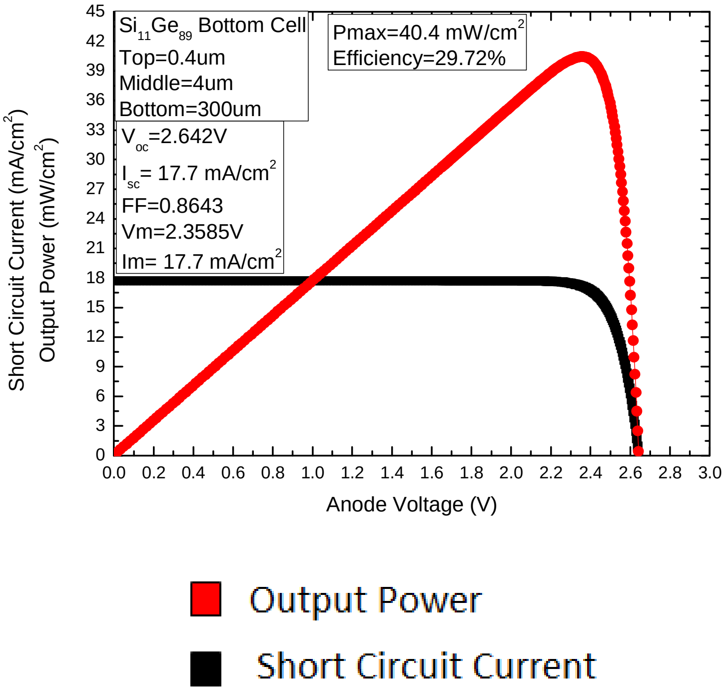

Figure 3.5 I-V characteristic of InGaP/GaAs/ $Si_{0.11}Ge_{0.89}$ tandem solar cell

The table below summarizes the important parameters from the plots.

	Top Cell (0.4um)	Middle Cell(4um)	Bottom cell(300um)	Tandem Cell
Voc (V)	1.4093	1.0216	0.2504	2.642
Isc (mA/cm^2)	17.8	17.7	48.5	17.7
Fill Factor	0.8928	0.8727	0.6815	0.8643
Efficiency (%)	16.44	11.61	6.09	29.72

Table 3.1 Operating point, Fill Factor and Efficiency of individual cells and the Tandem Cell for bottom cell configuration $Si_{0.11}Ge_{0.89}$

3.4 Parameter Variation

The current produced by a single cell depends on its thickness. As the base becomes thicker, the current produced becomes larger. In multijunction cells this principle is also true. However, the thicker a cell is, the more photons it absorbs and thus, less photons are allowed to pass through to the other cells bellow it. This “shadowing” affects greatly the lower cells and may lead them to photon starvation. Therefore, a thick top cell will cause the current produced by lower cells to decrease. In a multijunction configuration, each cell behaves like a current source. All these current sources are connected in series (Figure 3.6). Consequently, the total current produced by the structure is equal to the smallest current produced by the individual cells. Hence, a cell that is too thin or too shadowed will result in lower overall performance, creating a bottleneck for the others.

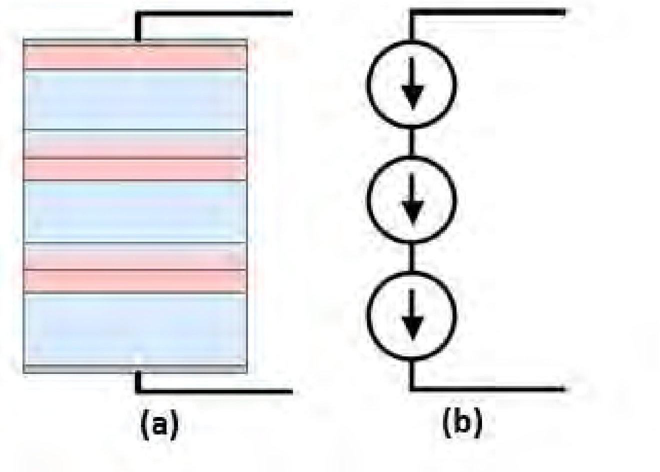

Figure 3.6 A multijunction solar cell (Fig a) as a set of current sources connected in series(Fig b)

3.4.1 Observing various trends

The following figure shows the variation of short-circuit current of the top cell vs. its thickness (Figure 3.7), for values of middle cell ranging from 1um to 9um. The top cell current is expected to increase with thickness since a thicker subcell will allow more photon absorption and hence greater photocurrent.

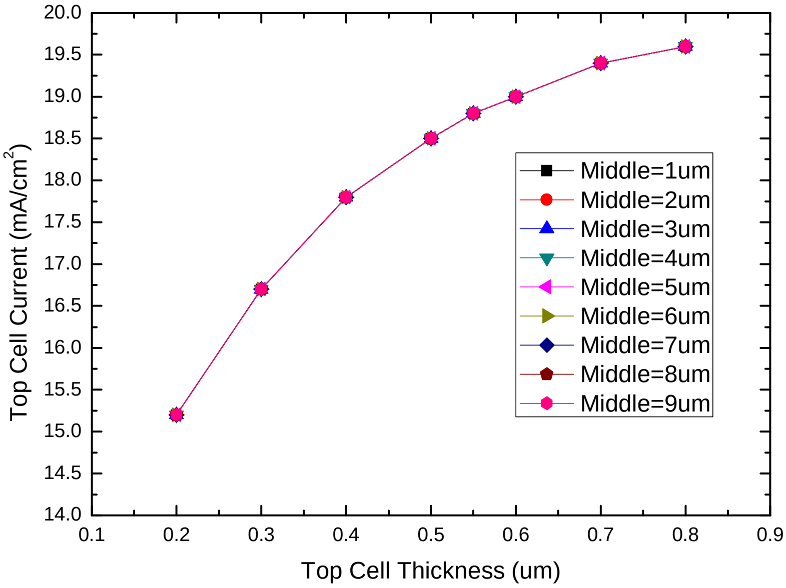

Figure 3.7 Top cell current vs top cell thickness

Here we see that the middle cell thickness has no effect on the top cell current which is expected because middle cell lies beneath the top cell. This is further illustrated in the following figure:

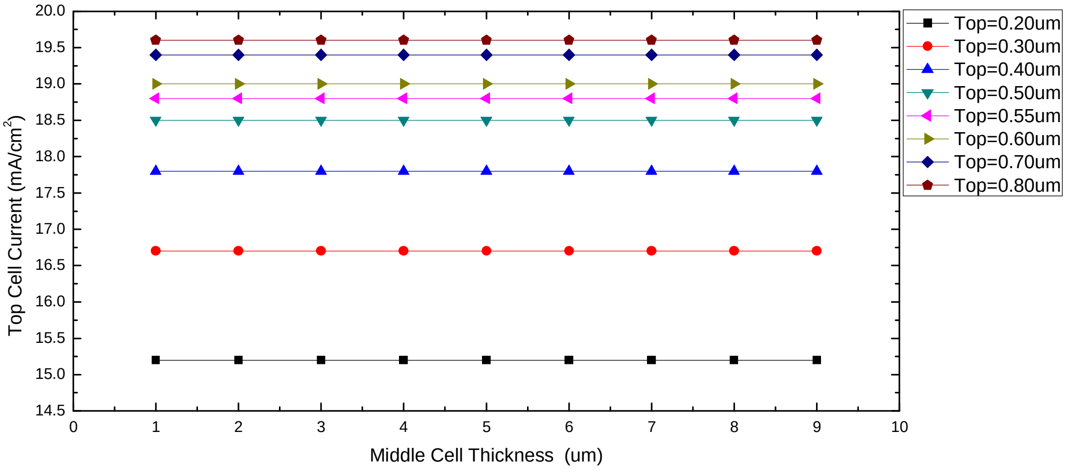

Figure 3.8 Top cell current vs middle cell thickness

Next, we see the variation of middle cell current when the top cell thickness is altered. Since the top cell is placed above the middle cell, its increasing thickness is expected to significantly reduce the current through the middle cell, because the thicker a cell is, the more photons it absorbs and thus, less photons are allowed to pass through to the other cells bellow it. This “shadowing” greatly affects the current of the middle cell.

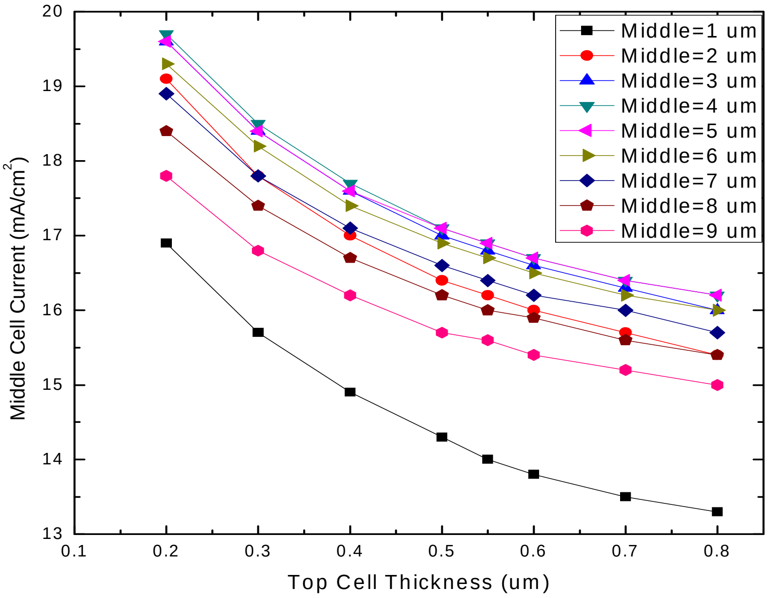

Figure 3.9 Middle cell current vs top cell thickness

Also, increasing the middle cell thickness will have a similar effect on the bottom cell current as shown in the next figure, Figure 3.10

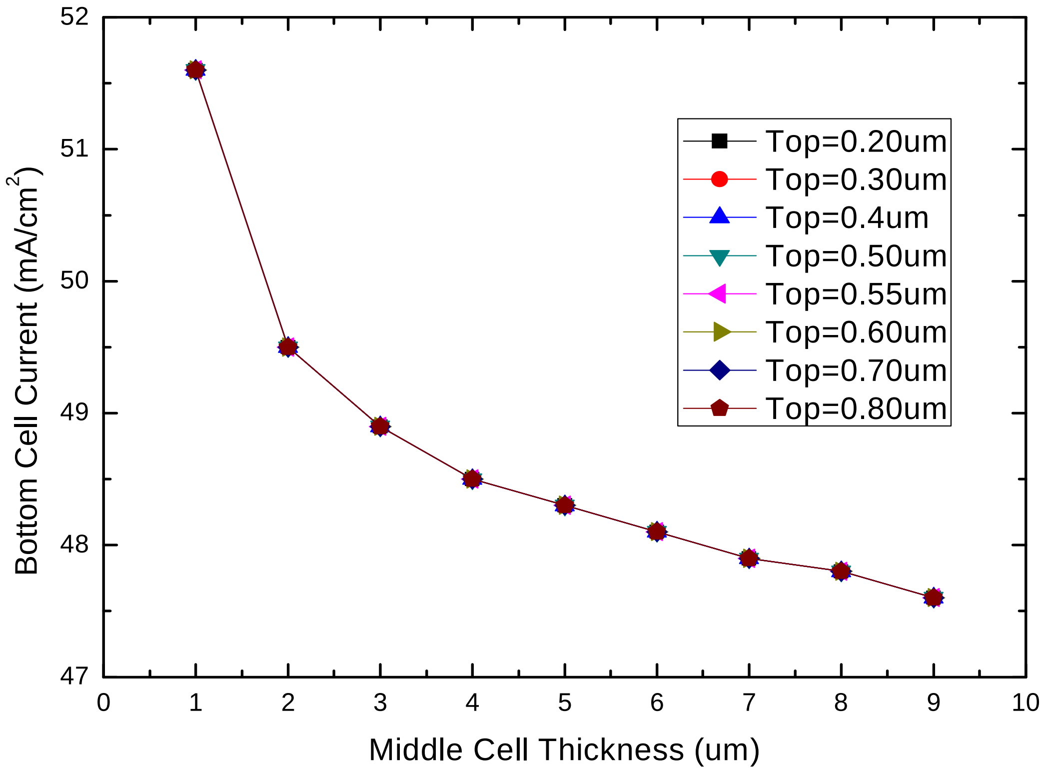

Figure 3.10 Bottom cell current vs. top cell thickness

Next we observe the effect of varying middle cell thickness with middle cell current.

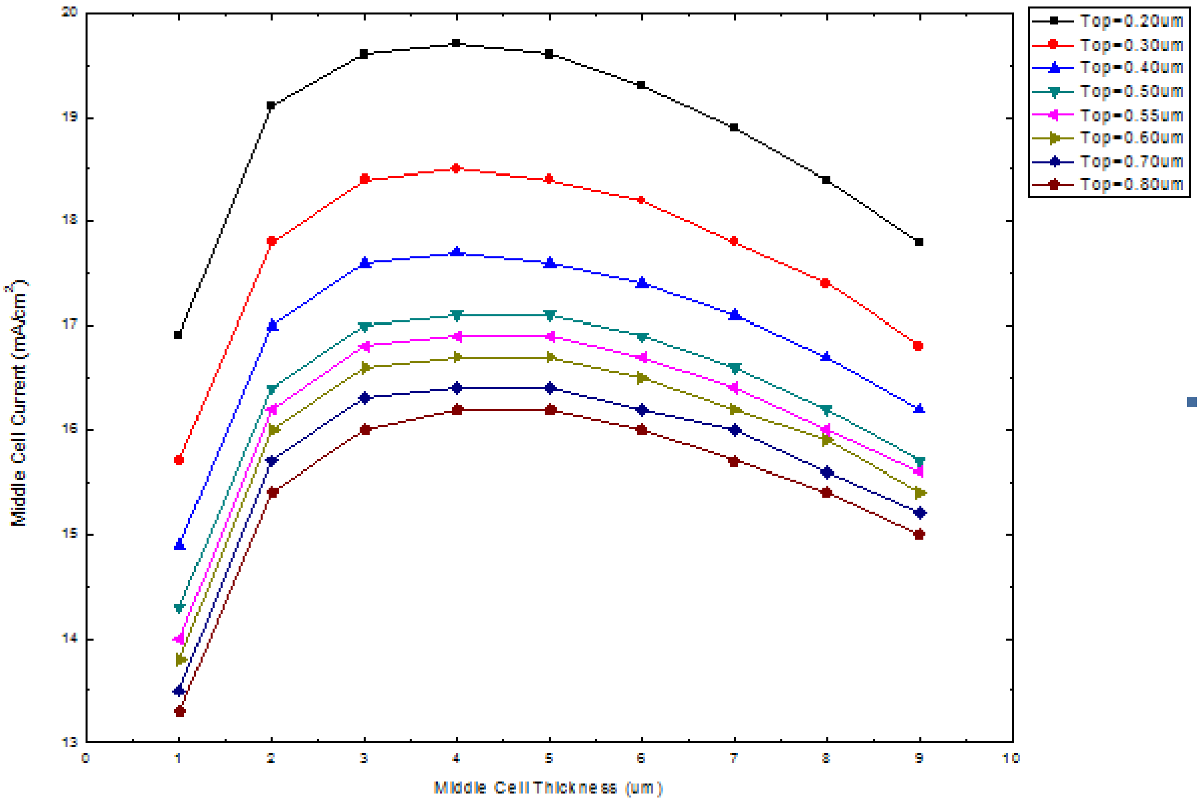

Figure 3.11 Middle cell current vs. middle cell thickness

Middle cell current increases with the increase of middle cell thickness up to a certain limit. This increase in current can be attributed to the increased absorption of photons due to the larger distance traveled by the photons. However, after a certain thickness the recombination in the middle cell region dominates and hence cell short circuit current starts to decrease.

3.4.2 Dimension optimization

In a triple junction solar cell, we know that the overall current is the minimum of the three individual subcell currents. For this reason, the dimensions need to be optimized to get the best possible current to in order to maximize efficiency. In Figure 3.12, there are eight plots for eight different top cell thickness (from 0.2um to 0.8 um) showing the variation of short circuit current with the middle cell thickness. The bottom cell current has a very high current due to its thickness, and hence is not taken into account here.

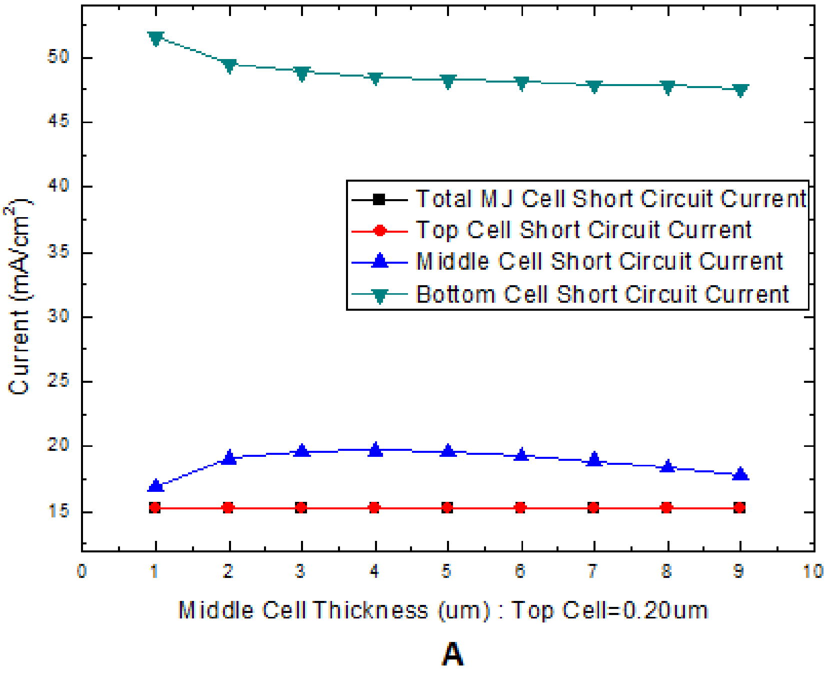

Figure 3.12: The short circuit current as a function of middle cell thickness for **A.** Top Cell Thickness= 0.2um

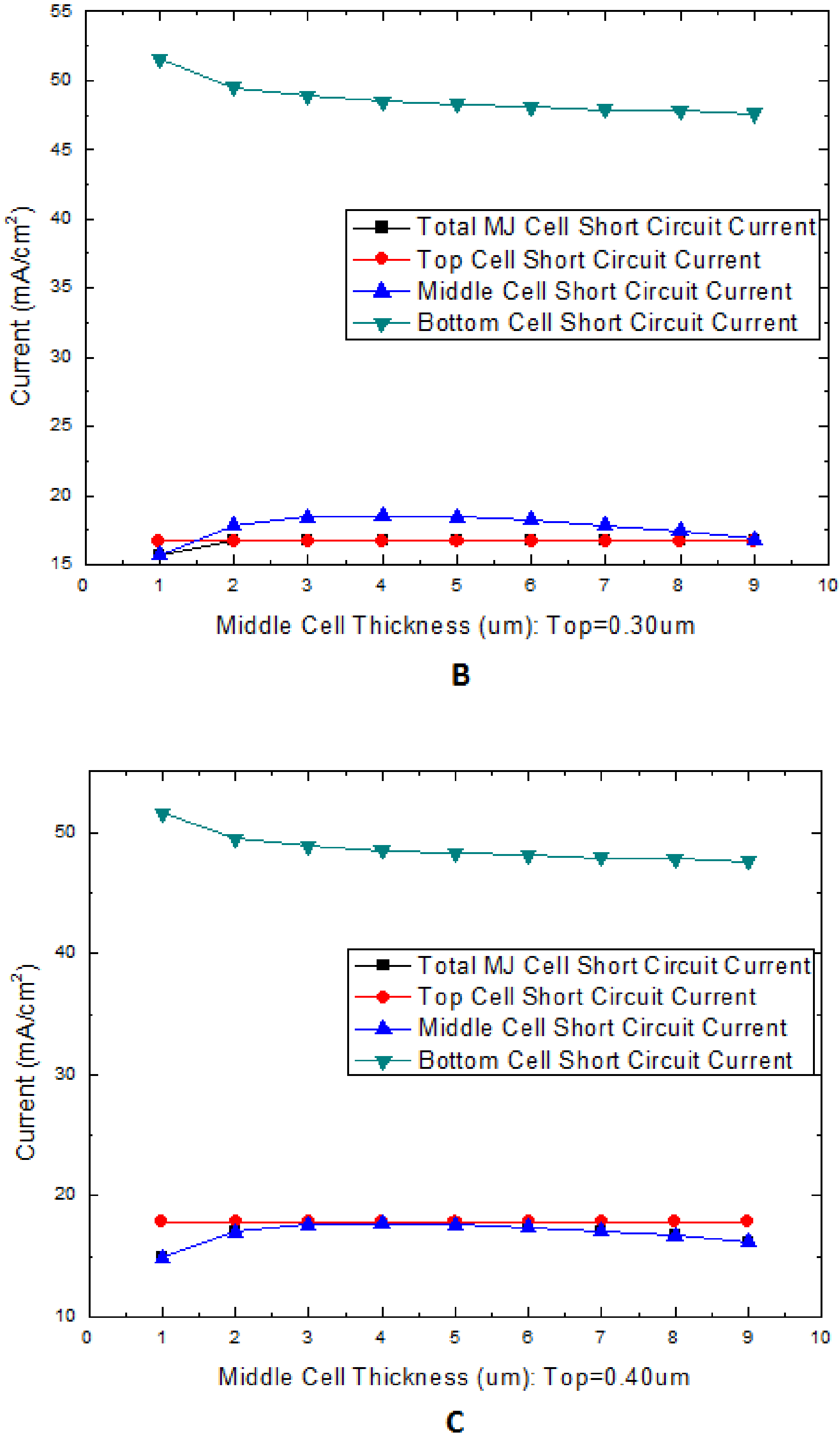

Figure 3.12: The short circuit current as a function of middle cell thickness for

B. Top Cell Thickness= 0.3um

C. Top Cell Thickness= 0.4um

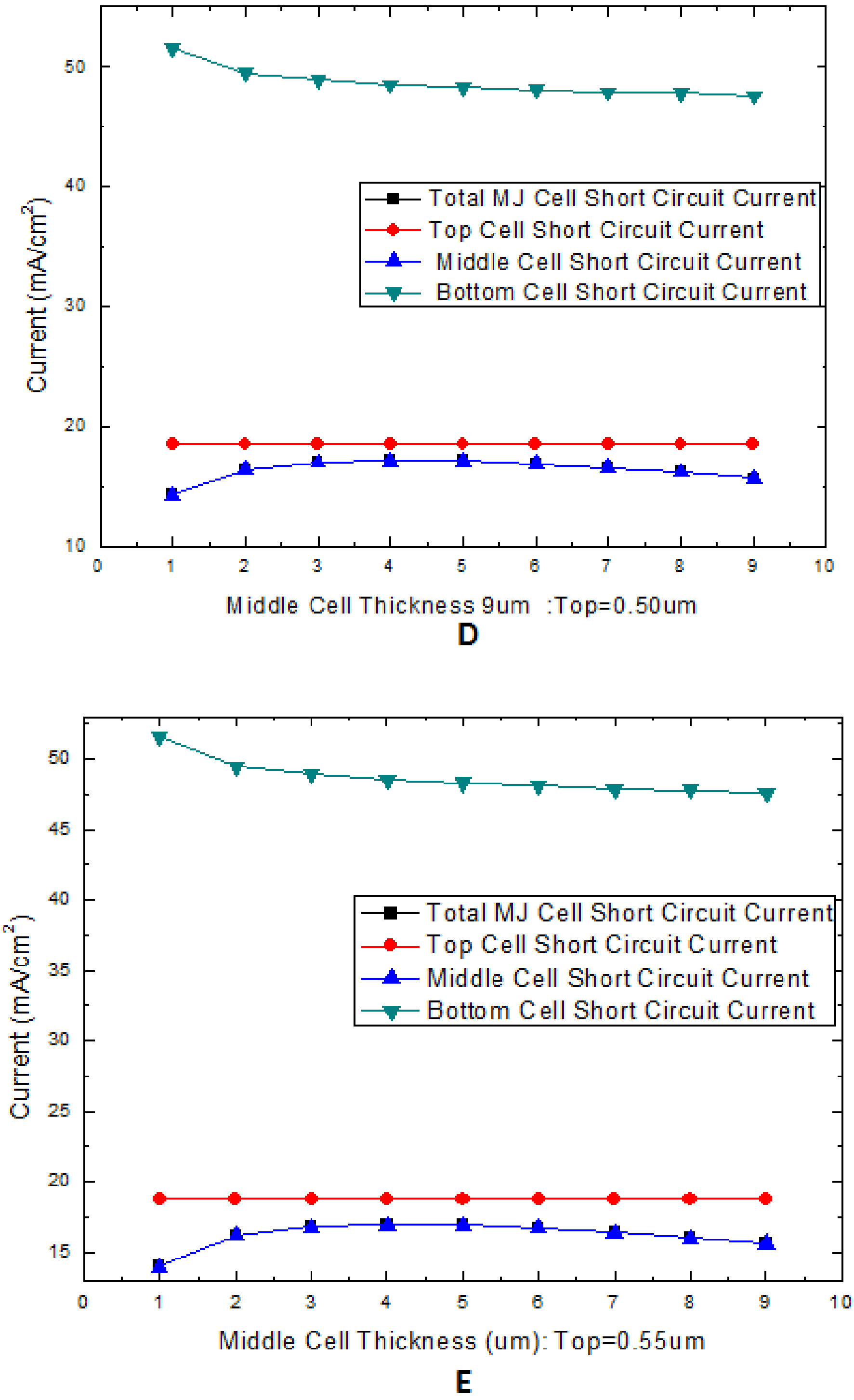

Figure 3.12: The short circuit current as a function of middle cell thickness for

D. Top Cell Thickness= 0.50um

E. Top Cell Thickness= 0.55um

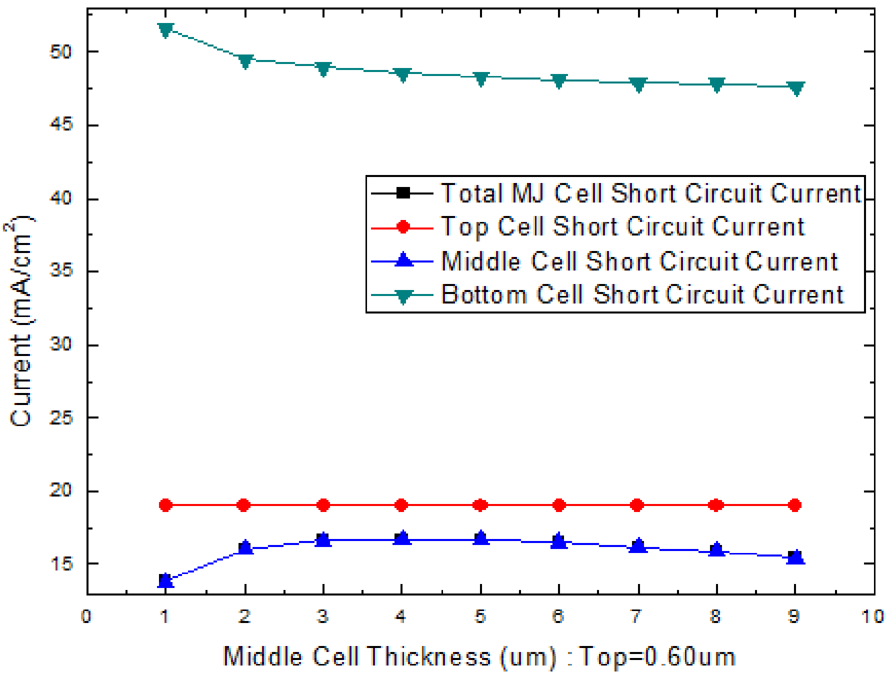

F

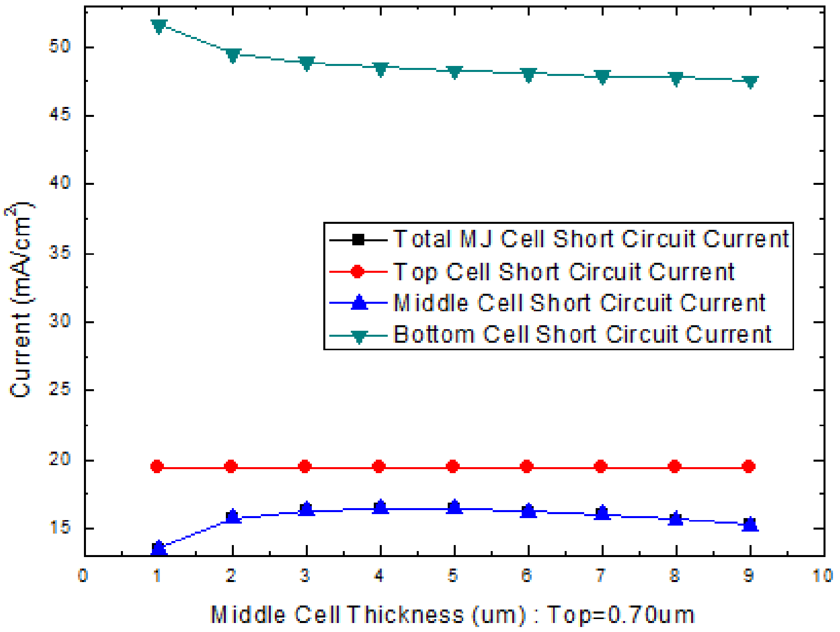

G

Figure 3.12: The short circuit current as a function of middle cell thickness for

F. Top Cell Thickness= 0.6um
G. Top Cell Thickness= 0.7um

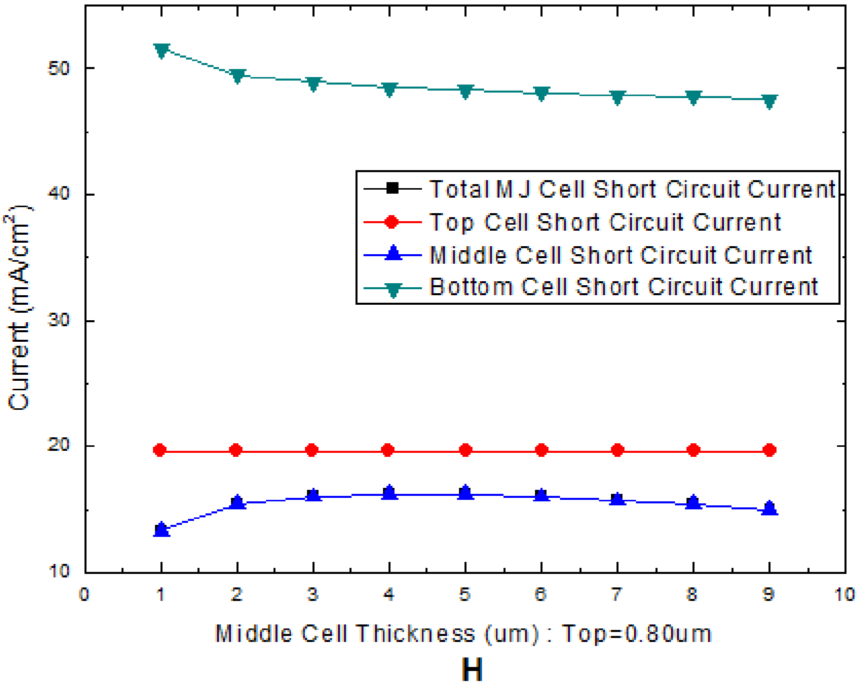

Figure 3.12: The short circuit current as a function of middle cell thickness for **H.** Top Cell Thickness= 0.8um

From the plots, we can see that the maximum short circuit current for the overall cell occurs in plot C for a top thickness of 0.40um and middle cell thickness of 4um.

This is further evident in Figure 3.13 when the variation of current is shown with respect to the top cell thickness. Here also separate plots are shown for different middle cell thickness (from 1um to 9um)

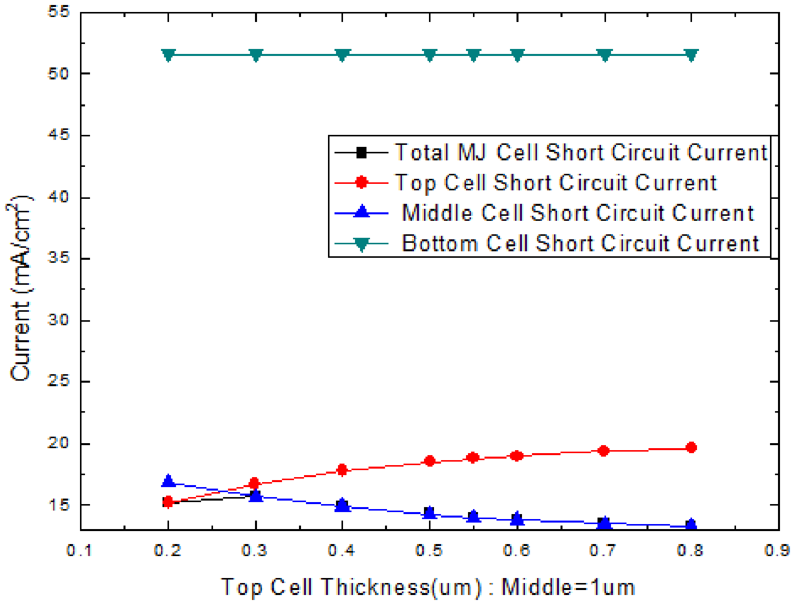

A

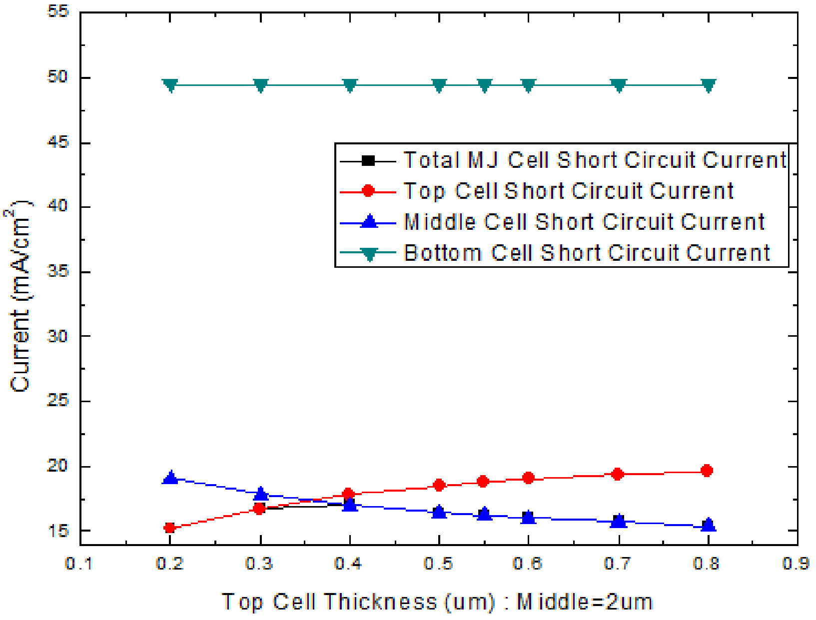

B

Figure 3.13: The short circuit current as a function of top cell thickness for
A. Middle Cell Thickness= 1um
B. Middle Cell Thickness=2um

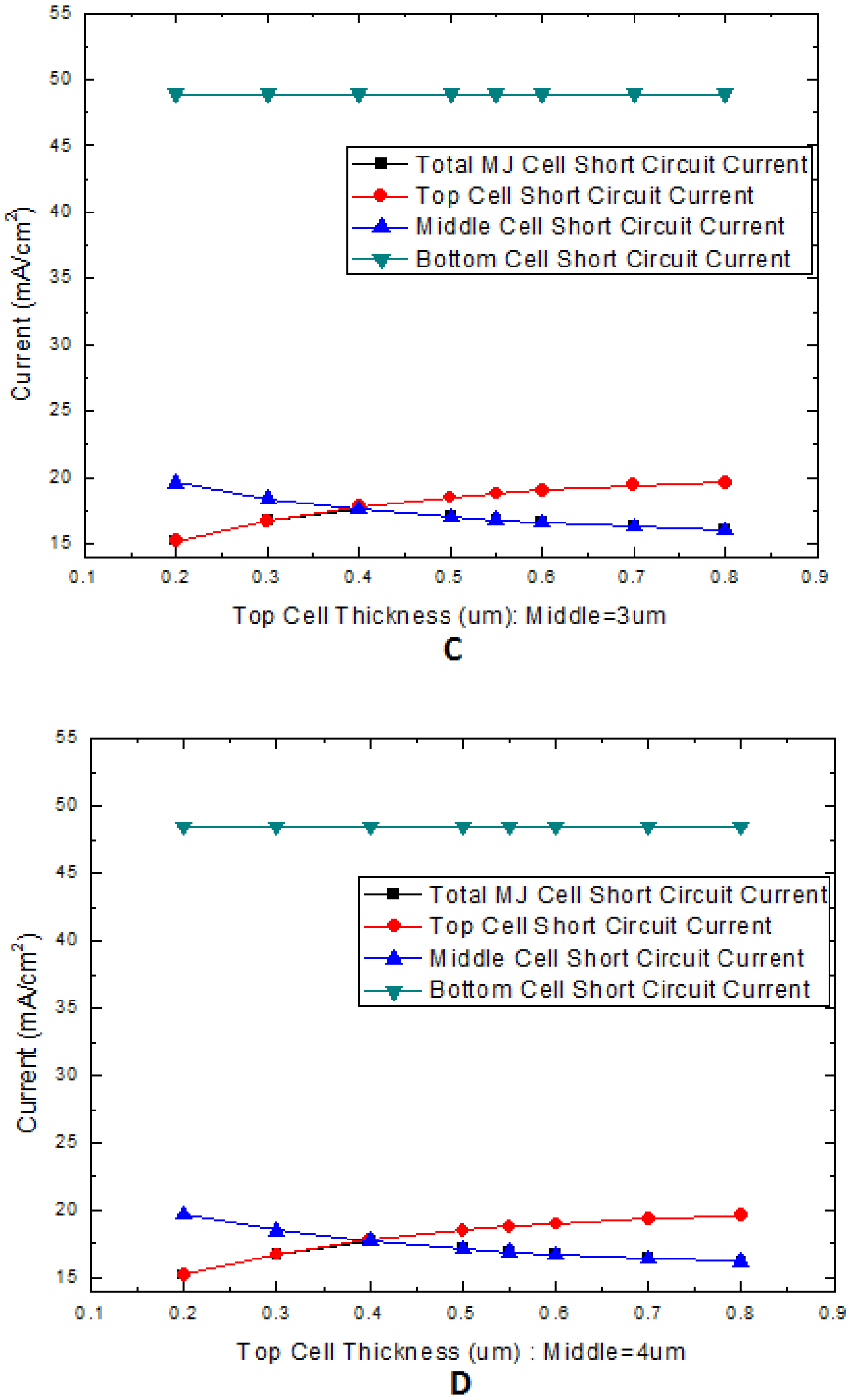

Figure 3.13: The short circuit current as a function of top cell thickness for
C. Middle Cell Thickness= 3um
D. Middle Cell Thickness= 4um

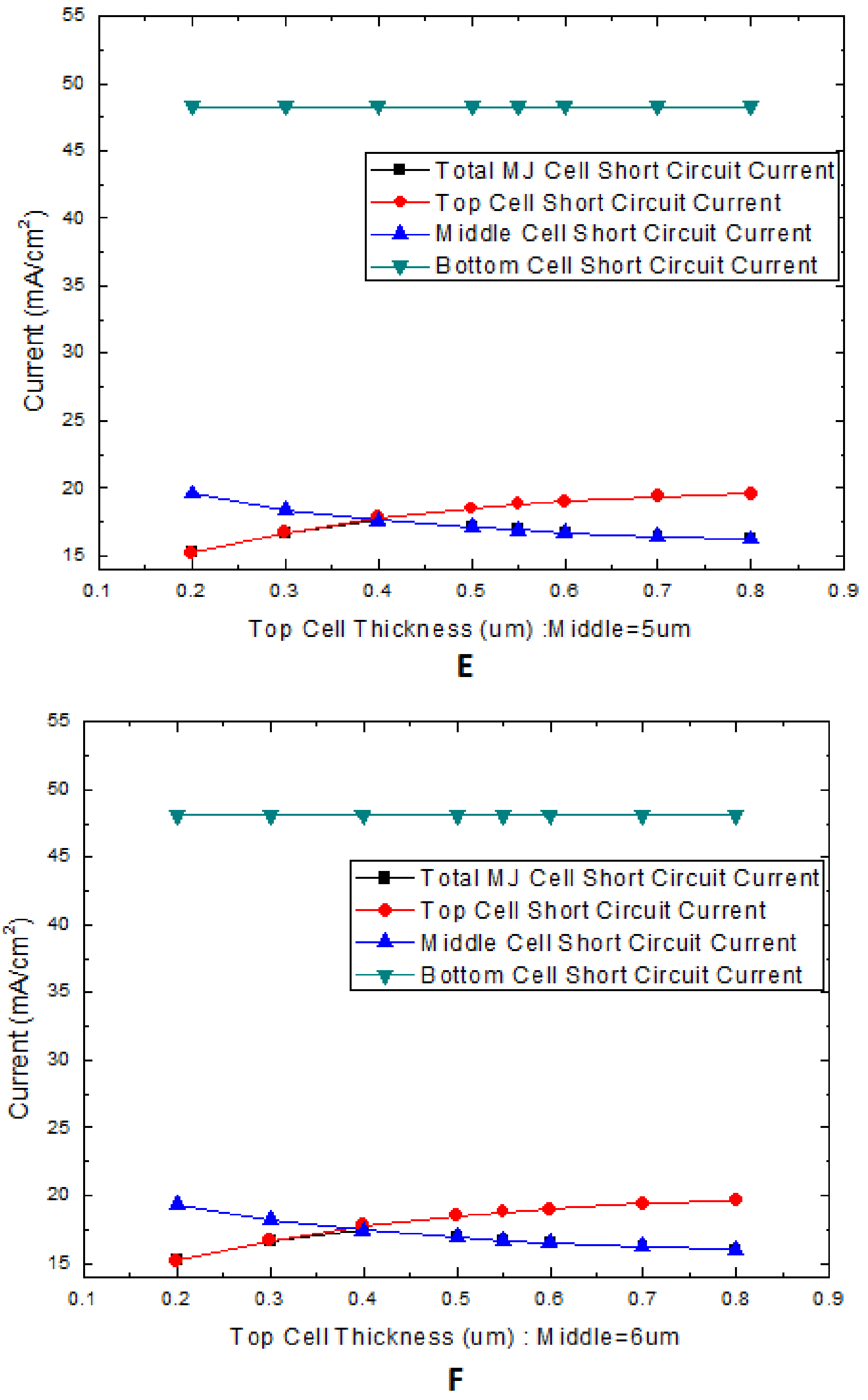

Figure 3.13: The short circuit current as a function of top cell thickness for

E. Middle Cell Thickness= 5um

F. Middle Cell Thickness= 6um

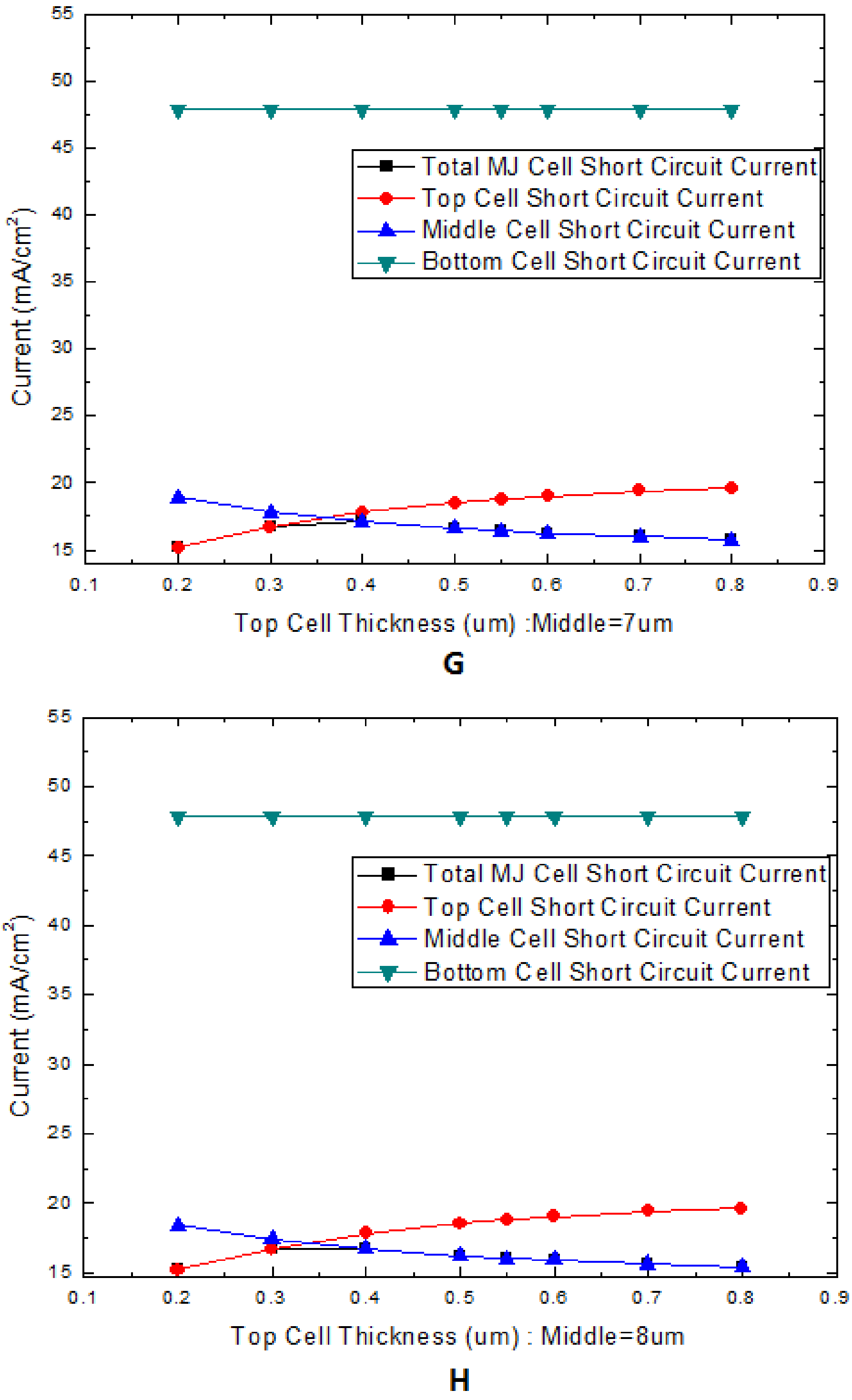

Figure 3.13: The short circuit current as a function of top cell thickness for

G. Middle Cell Thickness= 7um

H. Middle Cell Thickness= 8um

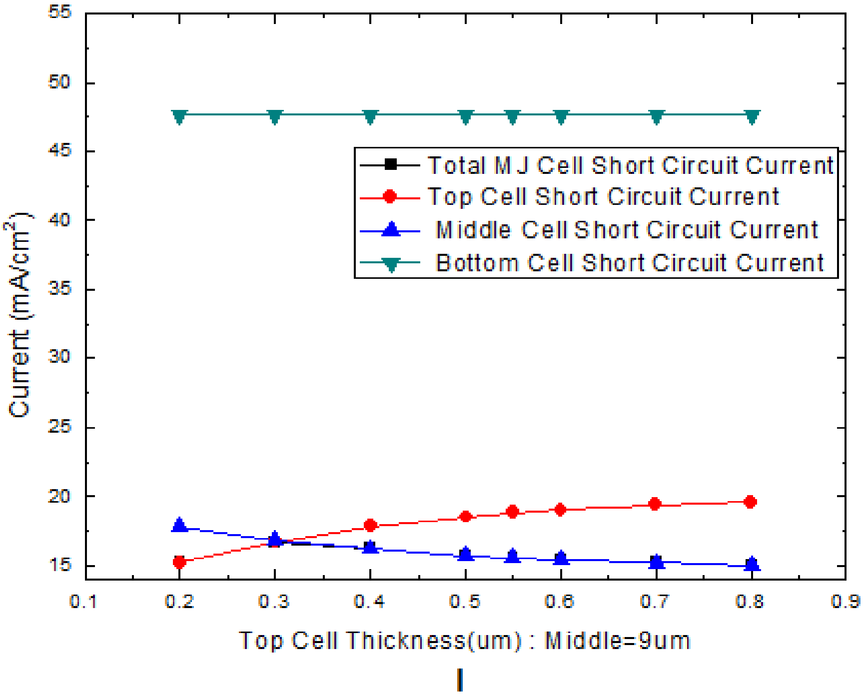

Figure 3.13: The short circuit current as a function of top cell thickness for
I. Middle Cell Thickness= 9um

From the above two figures we again see that the maximum Short Circuit current is found for a top cell thickness of 0.4um and middle cell thickness of 4um.

Thus we arrive to a conclusion that for the $Si_{0.11}Ge_{0.89}$ bottom cell composition, the highest short circuit current will be obtained when the middle cell thickness is 4um and top cell thickness is 0.4um.

In a similar way, the dimensions are optimized for all other compositions of bottom cell and the results are summarized in the table below:

	$Si_{0.11}Ge_{0.89}$	$Si_{0.20}Ge_{0.80}$	$Si_{0.28}Ge_{0.72}$	$Si_{0.65}Ge_{0.35}$	$Si_{0.85}Ge_{0.15}$	$Si_{0.98}Ge_{0.02}$
I_{sc}	0.0177	0.0177	0.0177	0.0177	0.0157	0.0096
t_{top}	0.40um	0.40um	0.40um	0.40um	0.30um	0.2um
t_{middle}	4um	4um	4um	4um	1um	1um
Efficiency	0.2972	0.2977	30.6	0.3225	0.2945	0.1886

Table 3.2 Overall short circuit current, top and middle cell thickness and overall efficiency for different composition of bottom cell

3.5 Different Bottom Cell Compositions

Here the effect of varying the bottom cell composition is observed and displayed in the graphs. The compositions considered are $Si_{0.11}Ge_{0.89}$, $Si_{0.20}Ge_{0.80}$, $Si_{0.28}Ge_{0.72}$, $Si_{0.65}Ge_{0.35}$, $Si_{0.85}Ge_{0.15}$ and $Si_{0.98}Ge_{0.02}$.

3.5.1 $Si_{0.11}Ge_{0.89}$

For this bottom cell composition, the overall short circuit current is observed as a function of top cell thickness, and then individual top cell current and middle cell current is also plotted as a function of top cell thickness. Finally the overall cell efficiency is shown as a function of the top cell thickness. In each of these plots we see a multiple curves, each one for a particular middle cell thickness.

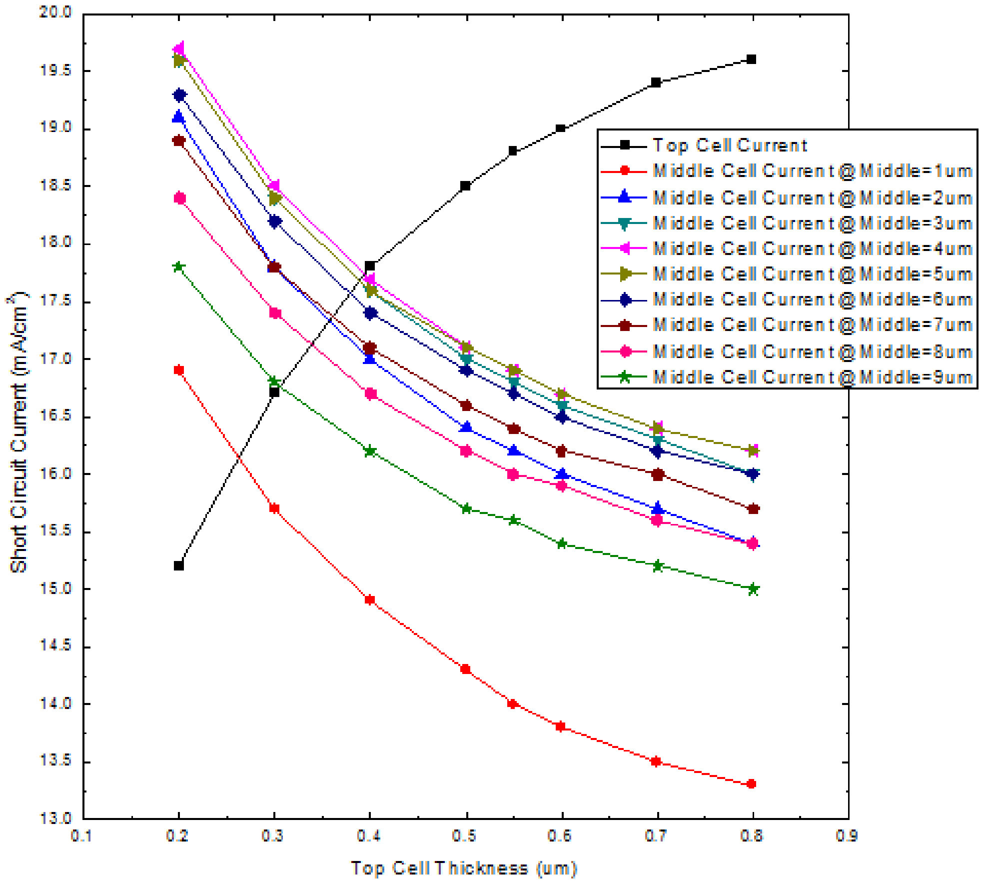

Figure 3.14 Short circuit current of top and middle cell as a function of top cell thickness (For bottom Cell Composition: $Si_{0.11}Ge_{0.89}$)

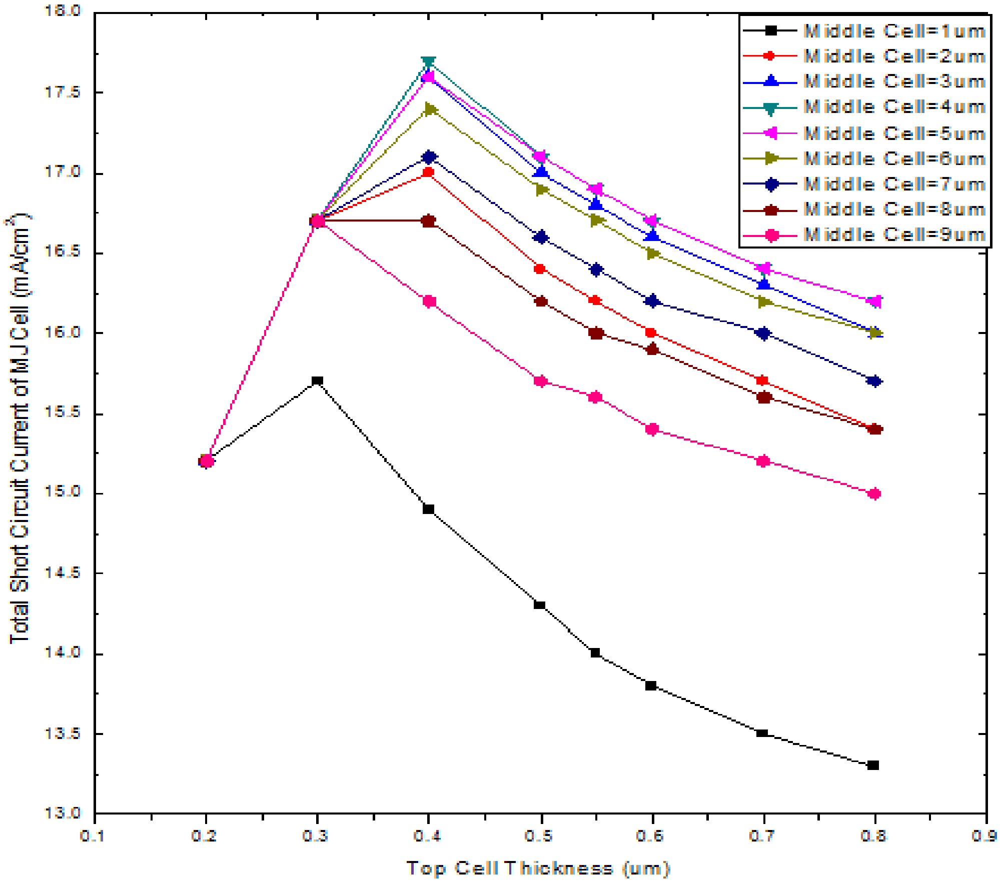

Figure 3.15 Overall Short circuit current of multijunction solar cell as a function of top cell thickness (For bottom Cell Composition: $Si_{0.11}Ge_{0.89}$)

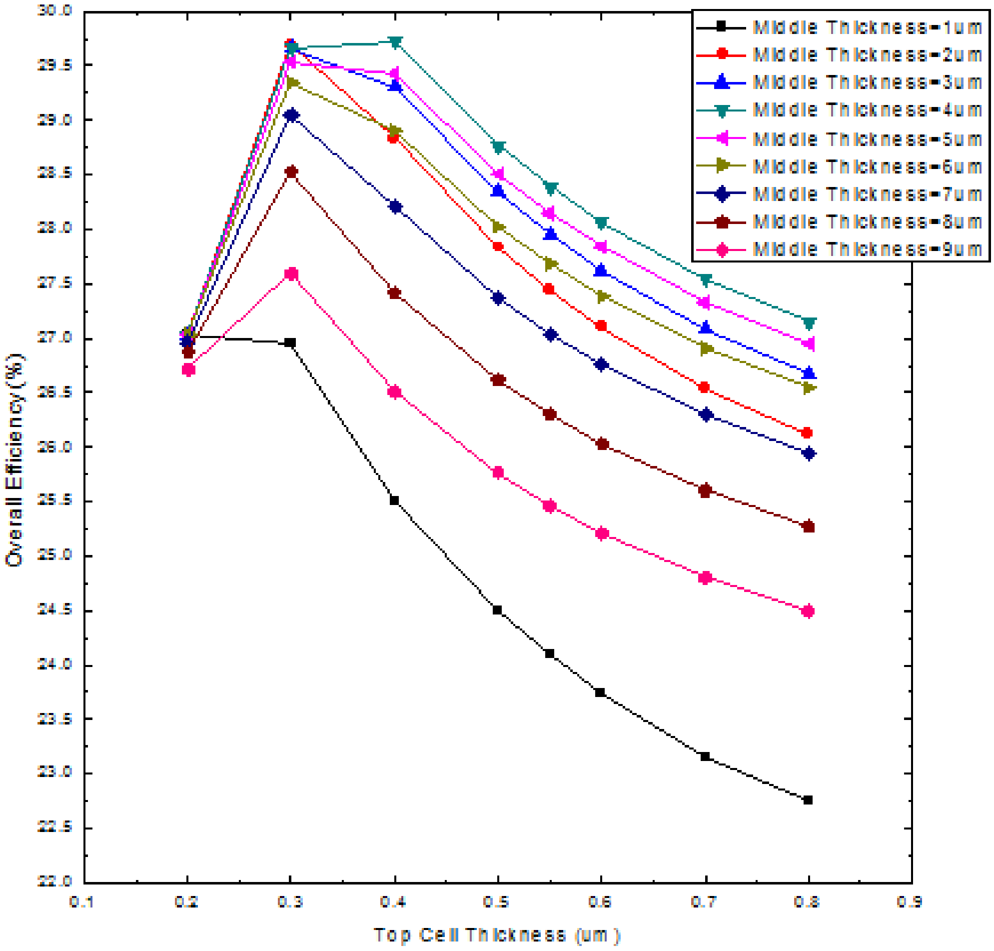

Figure 3.16 Overall efficiency of tandem solar cell as a function of top cell thickness (For bottom Cell Composition: $Si_{0.11}Ge_{0.89}$)

3.5.2 $Si_{0.20}Ge_{0.80}$

Here, again the overall short circuit current is observed as a function of top cell thickness, and then individual top cell current and middle cell current is also plotted as a function of top cell thickness. Finally the overall cell efficiency is shown as a function of the top cell thickness. In each of these plots we see a multiple curves, each one for a particular middle cell thickness.

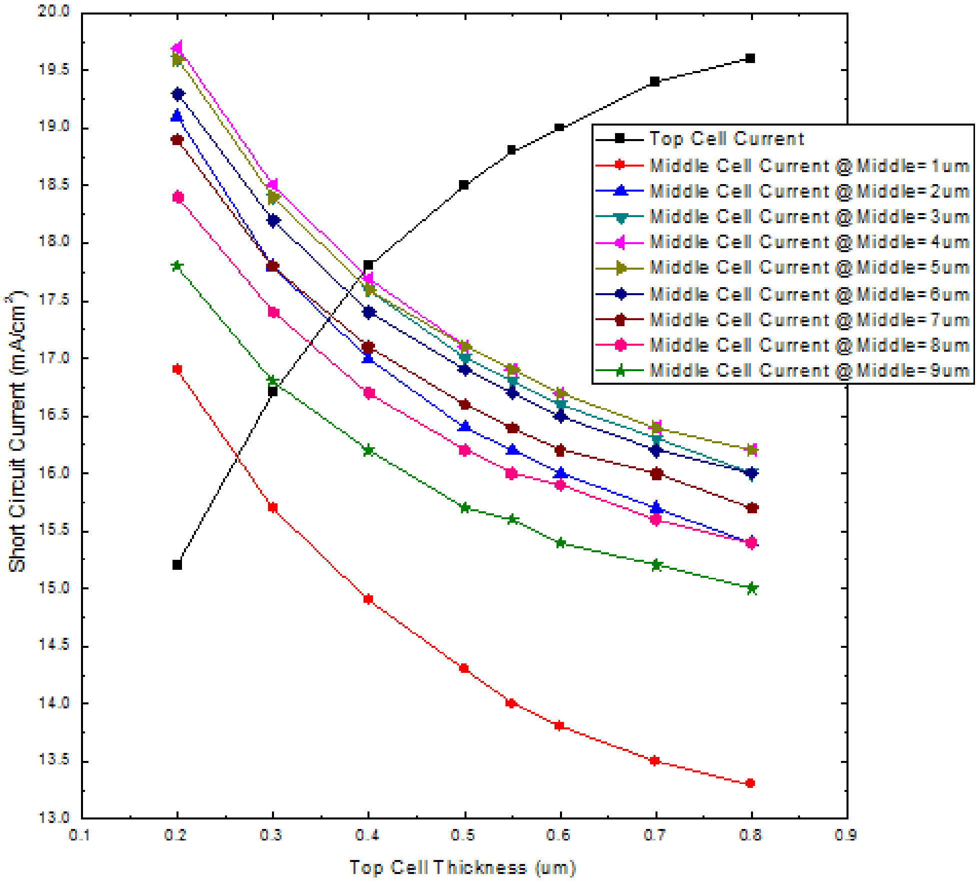

Figure 3.17 Short circuit current of top and middle cell as a function of top cell thickness (For bottom Cell Composition: $Si_{0.20}Ge_{0.80}$)

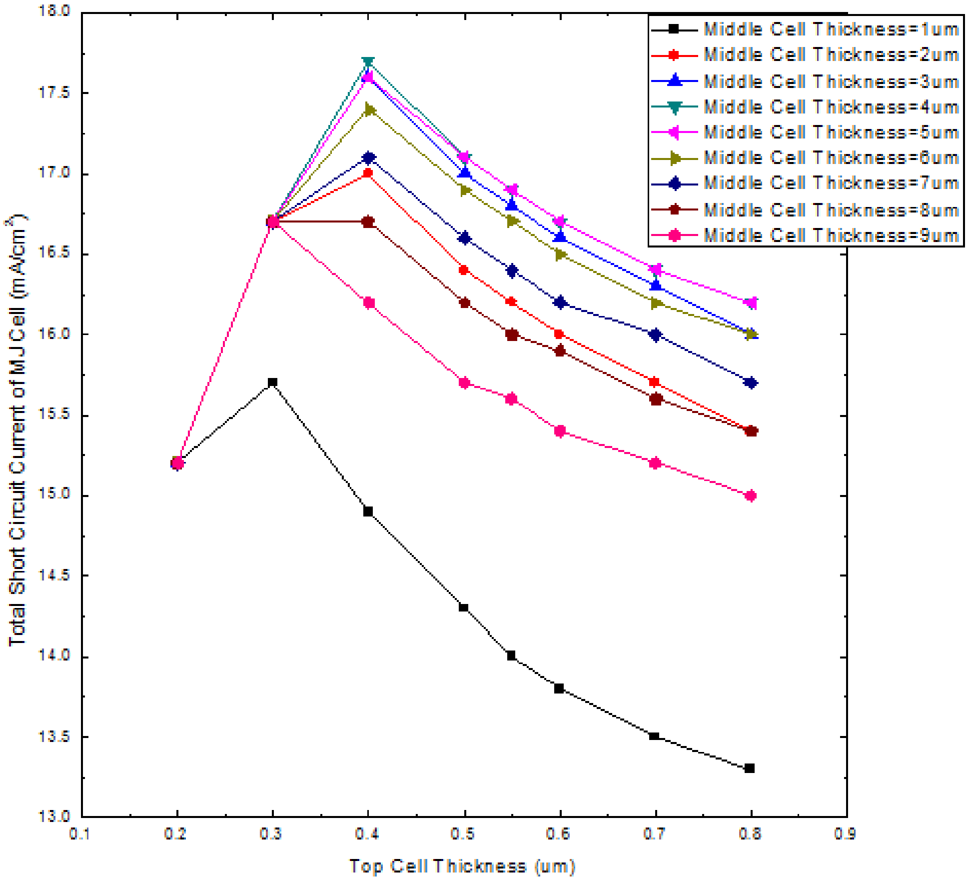

Figure 3.18 Overall Short circuit current of multijunction solar cell as a function of top cell thickness (For bottom Cell Composition: $Si_{0.20}Ge_{0.80}$)

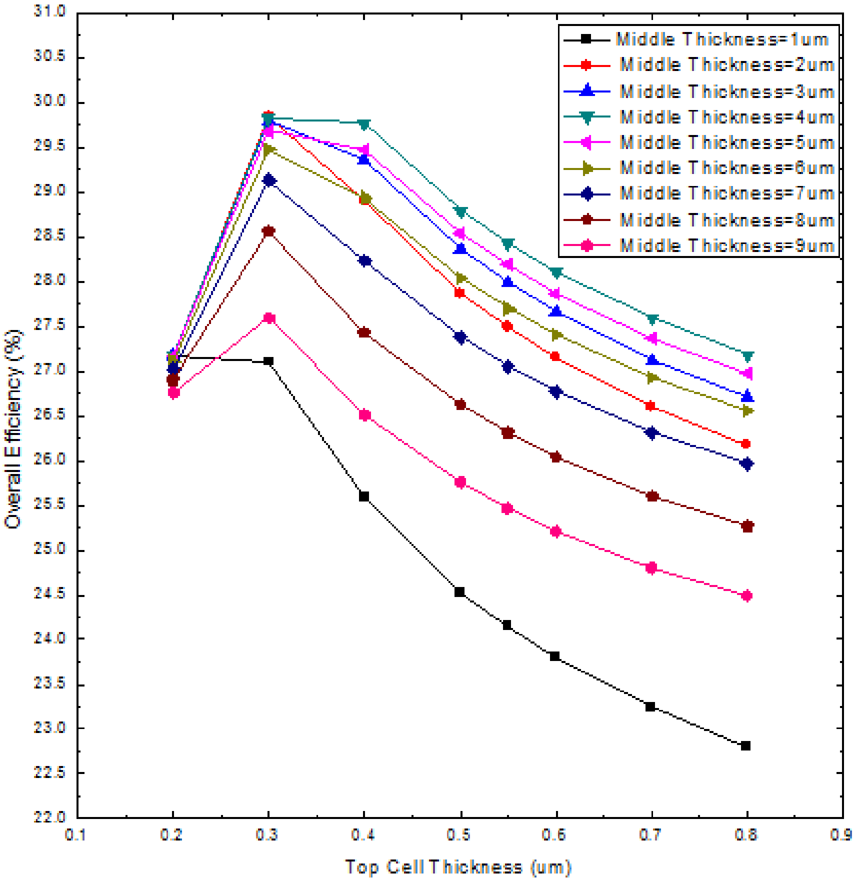

Figure 3.19 Overall efficiency of tandem solar cell as a function of top cell thickness (For bottom Cell Composition: $Si_{0.20}Ge_{0.80}$)

3.5.3 $Si_{0.28}Ge_{0.72}$

Here, again the overall short circuit current is observed as a function of top cell thickness, and then individual top cell current and middle cell current is also plotted as a function of top cell thickness. Finally the overall cell efficiency is shown as a function of the top cell thickness. In each of these plots we see a multiple curves, each one for a particular middle cell thickness.

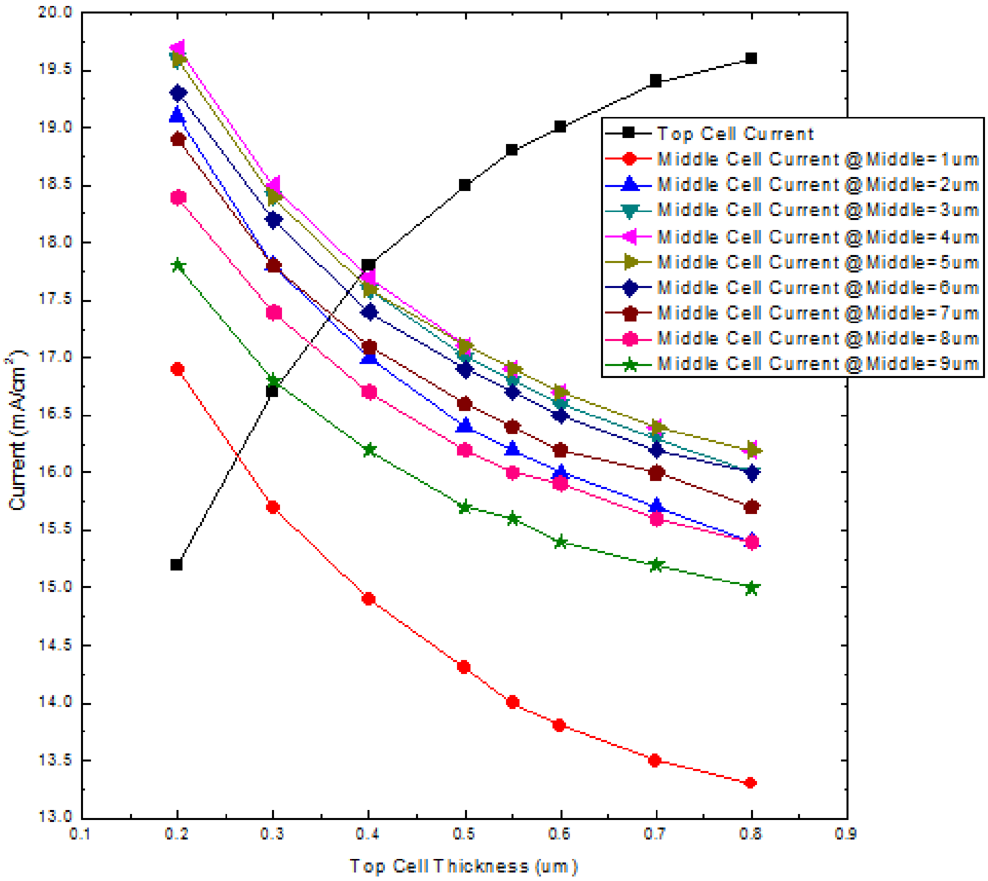

Figure 3.20 Short circuit current of top and middle cell as a function of top cell thickness (For bottom Cell Composition: $Si_{0.28}Ge_{0.72}$)

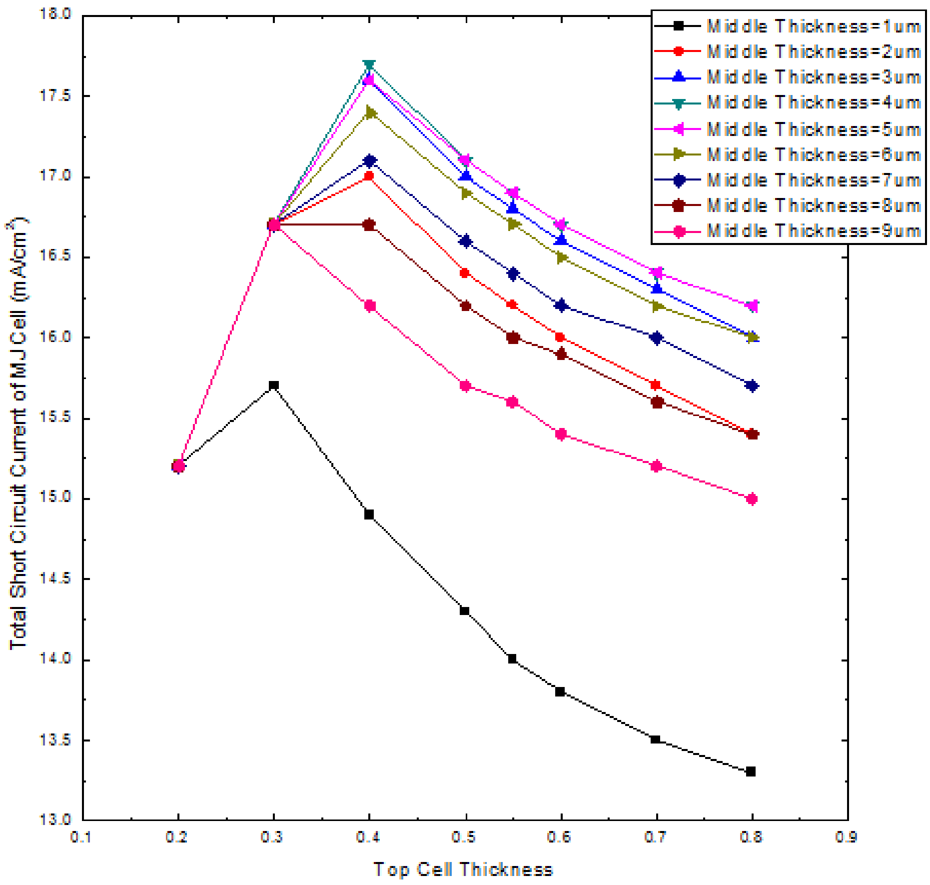

Figure 3.21 Overall Short circuit current of multijunction solar cell as a function of top cell thickness(For bottom Cell Composition: $Si_{0.28}Ge_{0.72}$)

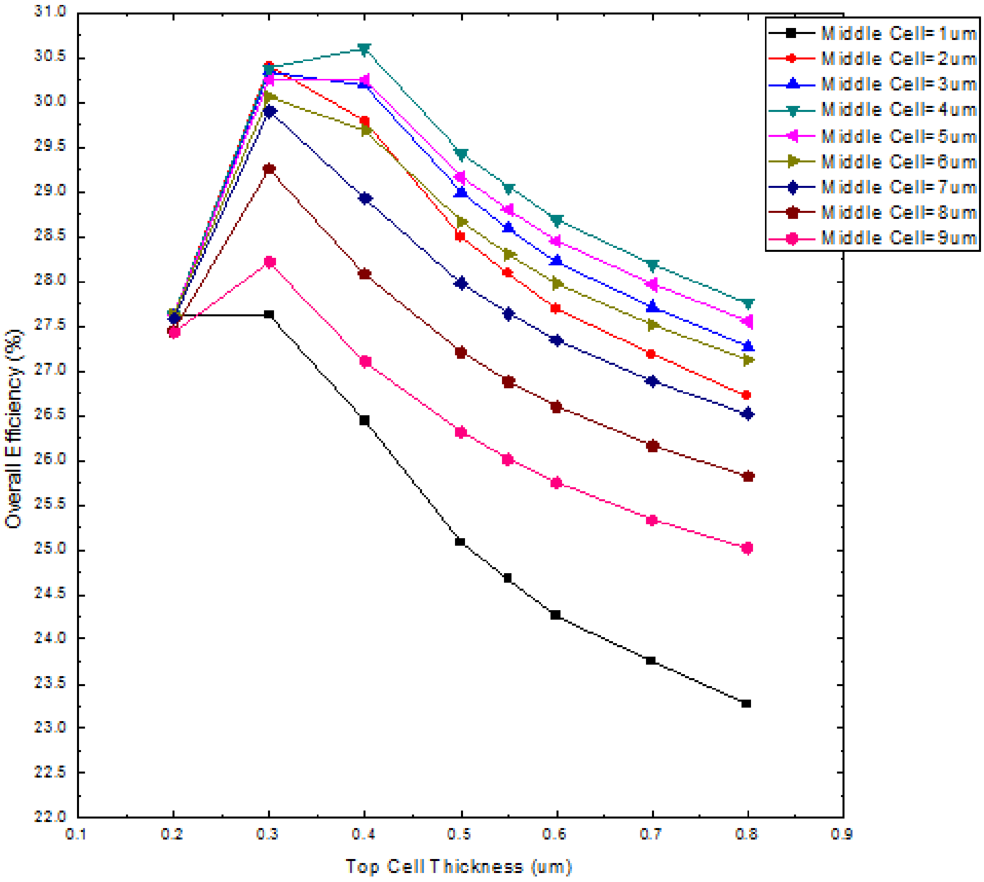

Figure 3.22 Overall efficiency of tandem solar cell as a function of top cell thickness (For bottom Cell Composition: $Si_{0.28}Ge_{0.72}$)

3.5.4 $Si_{0.65}Ge_{0.35}$

Here, again the overall short circuit current is observed as a function of top cell thickness, and then individual top cell current and middle cell current is also plotted as a function of top cell thickness. Finally the overall cell efficiency is shown as a function of the top cell thickness. In each of these plots we see a multiple curves, each one for a particular middle cell thickness.

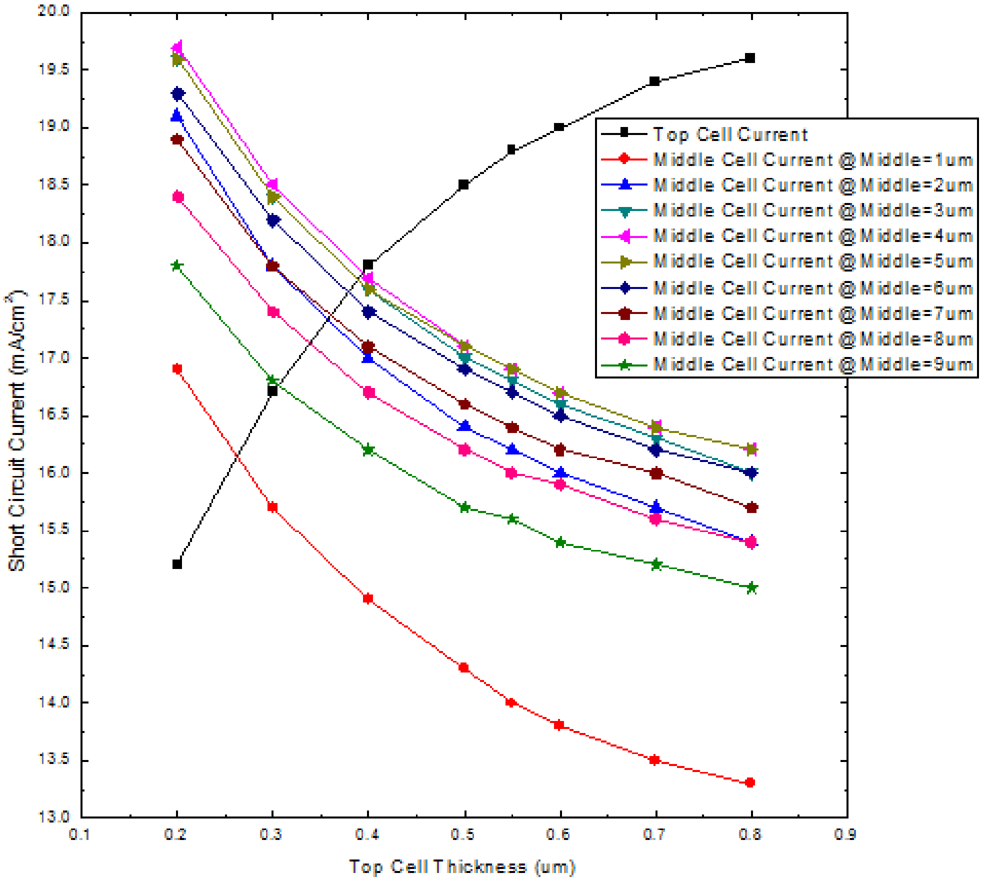

Figure 3.23 Short circuit current of top and middle cell as a function of top cell thickness (For bottom Cell Composition: $Si_{0.65}Ge_{0.35}$)

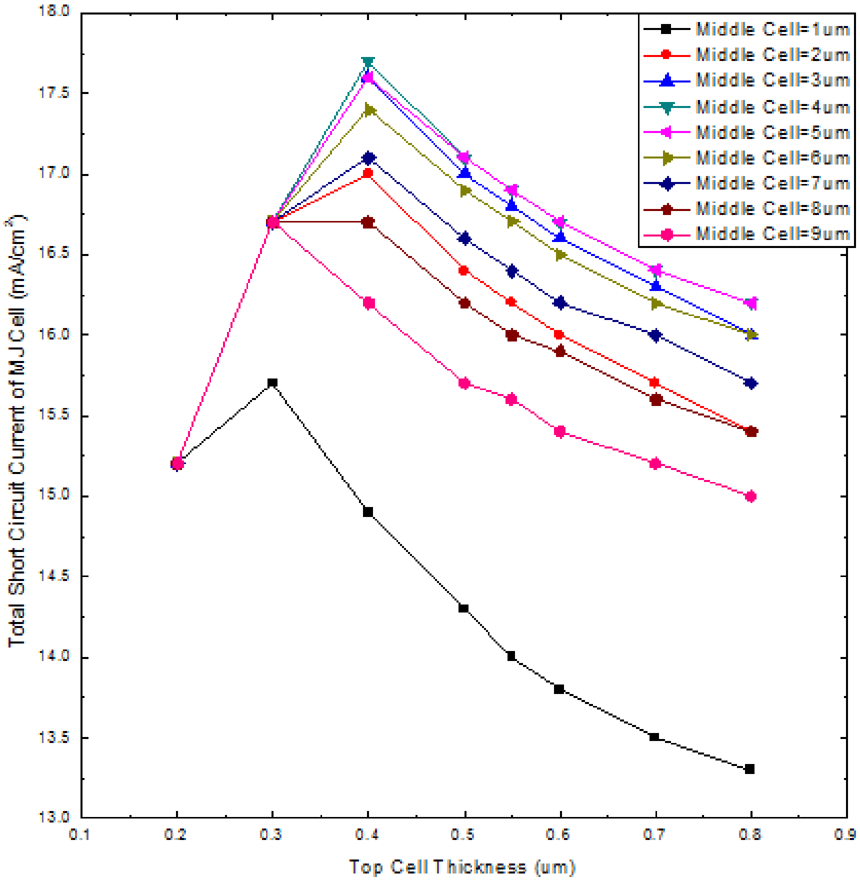

Figure 3.24 Overall Short circuit current of multijunction solar cell as a function of top cell thickness (For bottom Cell Composition: $Si_{0.65}Ge_{0.35}$)

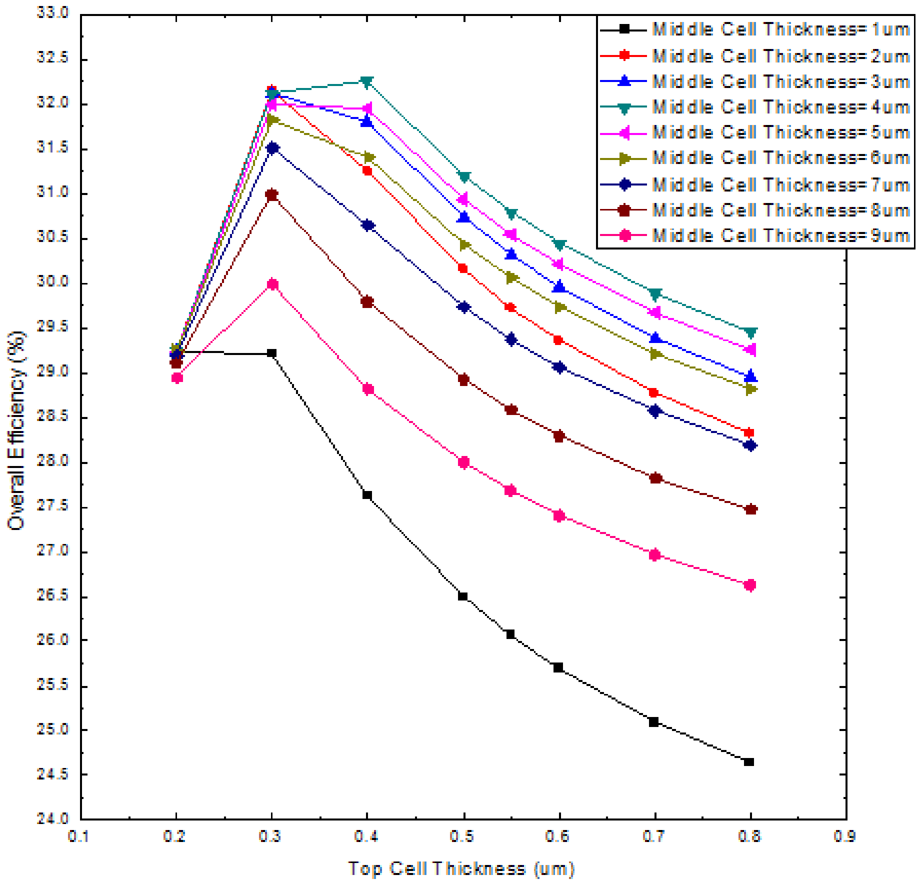

Figure 3.25 Overall efficiency of tandem solar cell as a function of top cell thickness (For bottom Cell Composition: $Si_{0.65}Ge_{0.35}$)

3.5.5 $Si_{0.85}Ge_{0.15}$

Here, again the overall short circuit current is observed as a function of top cell thickness, and then individual top cell current and middle cell current is also plotted as a function of top cell thickness. Finally the overall cell efficiency is shown as a function of the top cell thickness. In each of these plots we see a multiple curves, each one for a particular middle cell thickness.

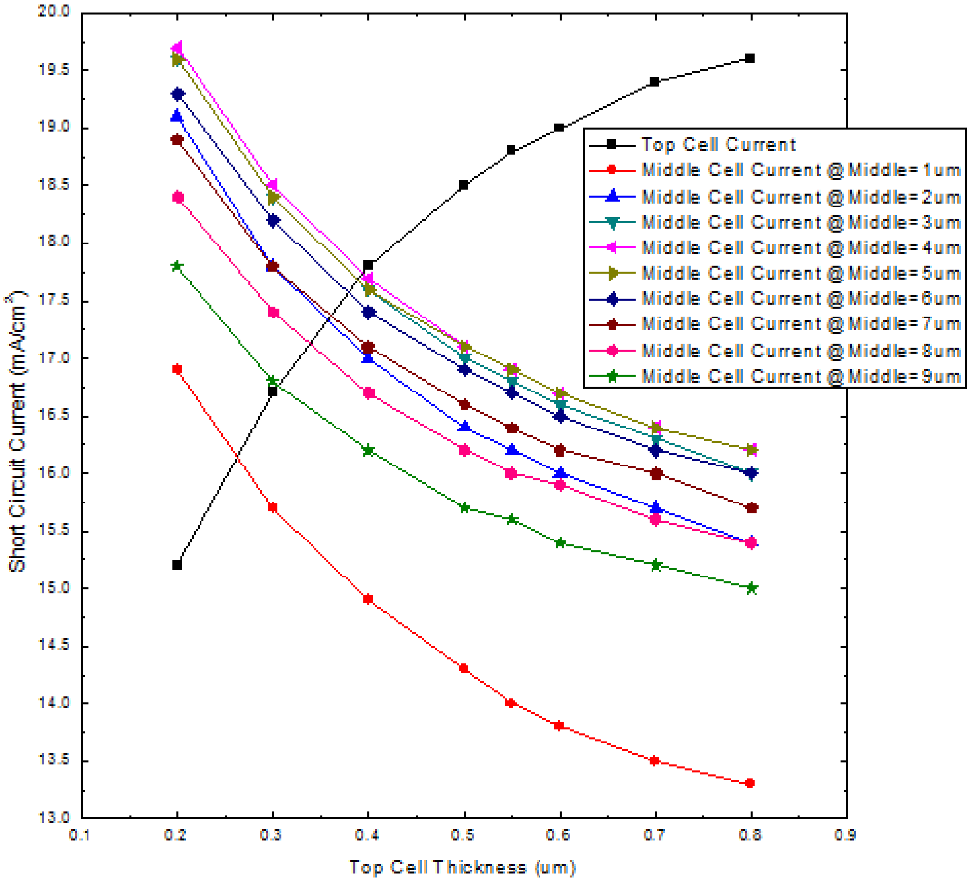

Figure 3.26 Short circuit current of top and middle cell as a function of top cell thickness (For bottom Cell Composition: $Si_{0.85}Ge_{0.15}$)

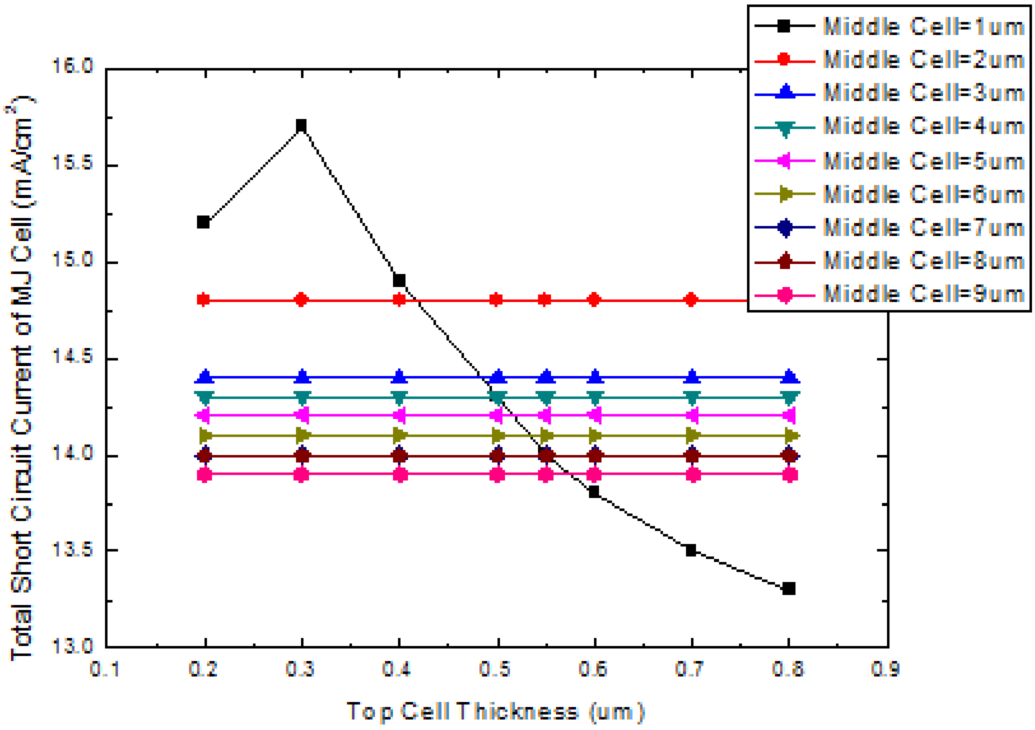

Figure 3.27 Overall Short circuit current of multijunction solar cell as a function of top cell thickness(For bottom Cell Composition: $Si_{0.85}Ge_{0.15}$)

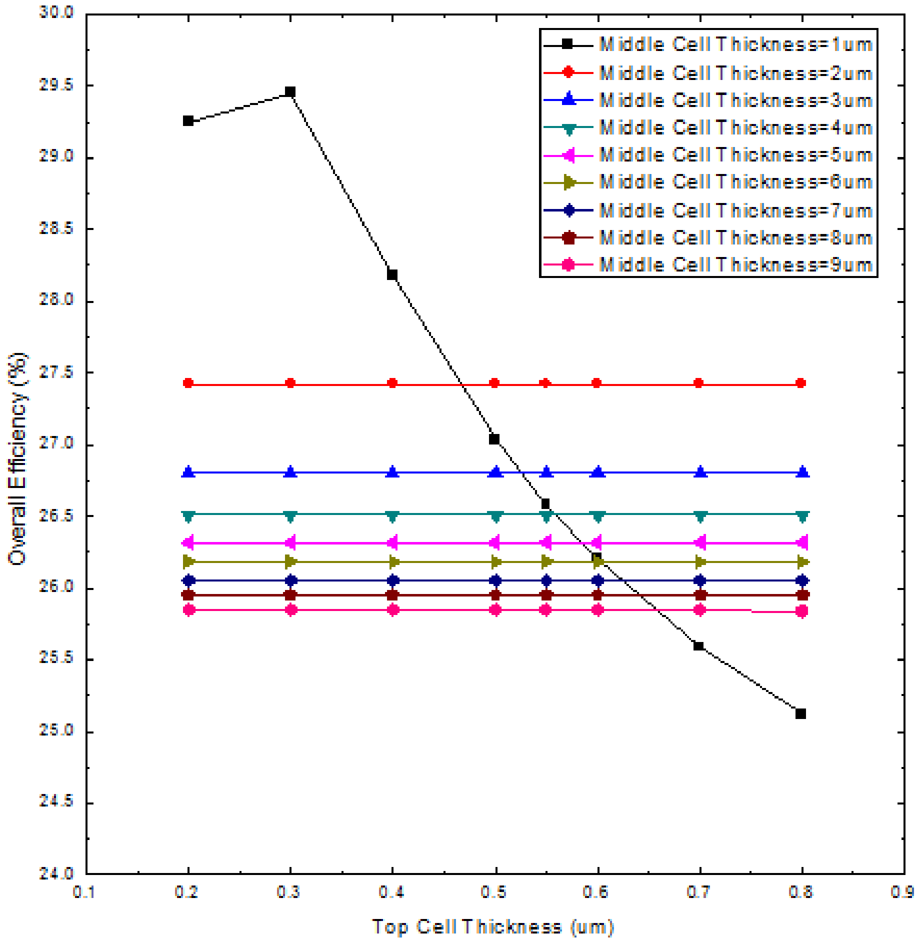

Figure 3.28 Overall efficiency of tandem solar cell as a function of top cell thickness (For bottom Cell Composition: $Si_{0.85}Ge_{0.15}$)

3.5.6 Si$_{0.98}$Ge$_{0.02}$

Here, again the overall short circuit current is observed as a function of top cell thickness, and then individual top cell current and middle cell current is also plotted as a function of top cell thickness. Finally the overall cell efficiency is shown as a function of the top cell thickness. In each of these plots we see a multiple curves, each one for a particular middle cell thickness.

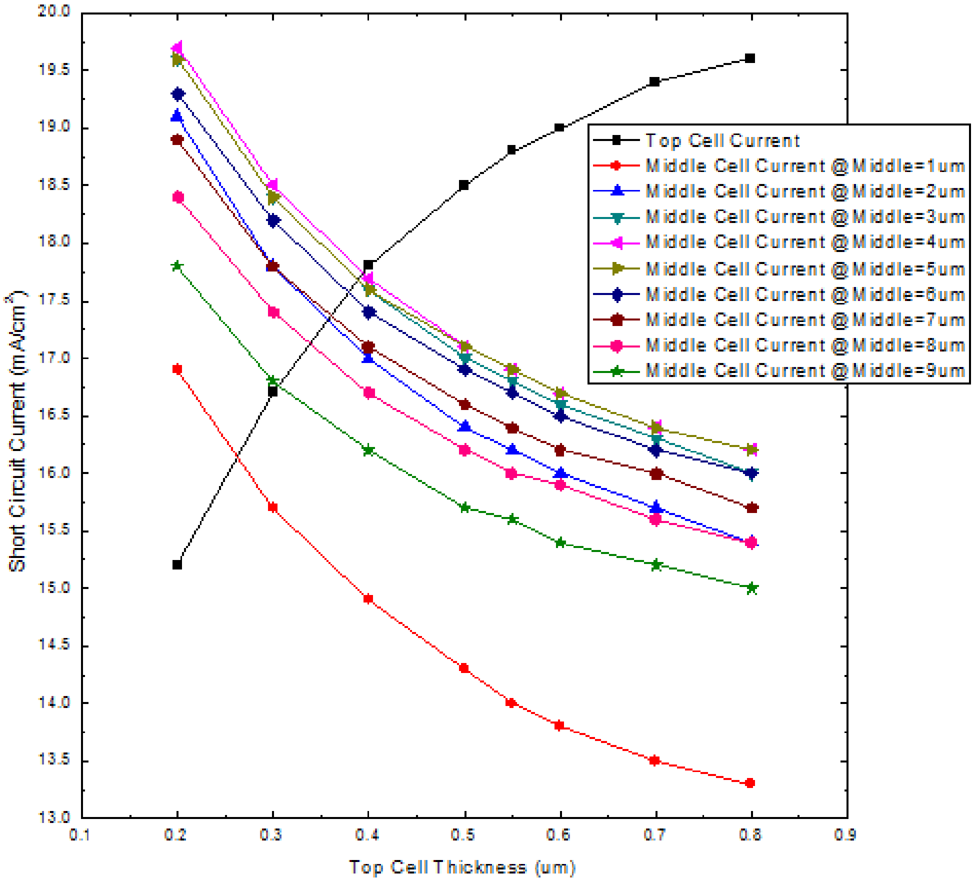

Figure 3.29 Short circuit current of top and middle cell as a function of top cell thickness (For bottom Cell Composition: Si$_{0.98}$Ge$_{0.02}$)

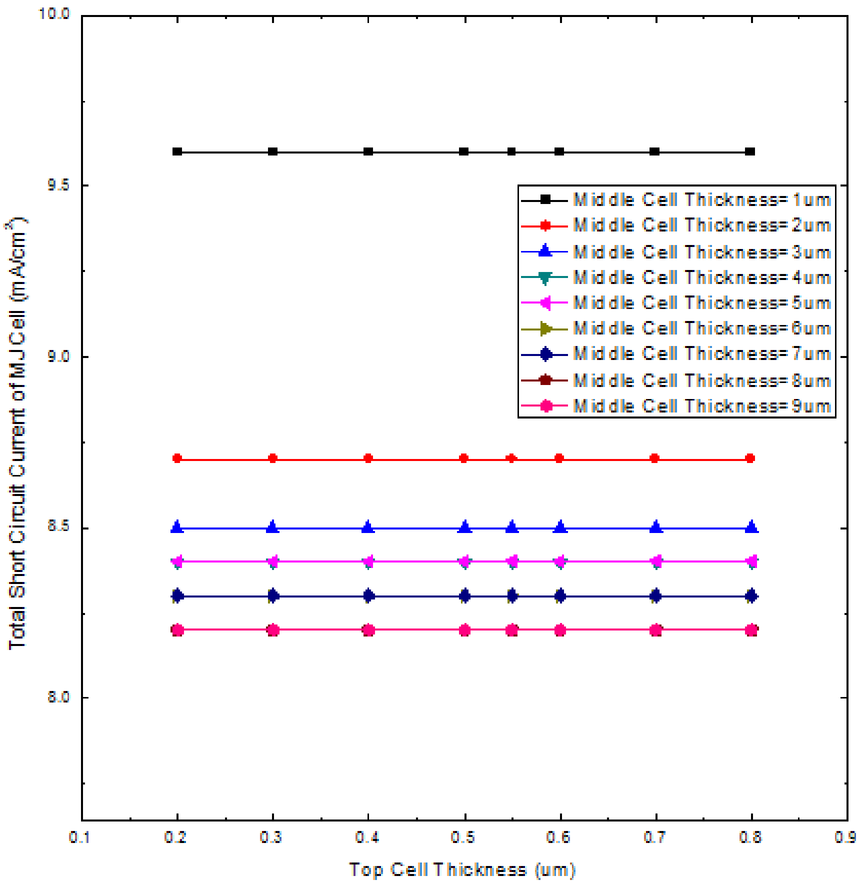

Figure 3.30 Overall Short circuit current of multijunction solar cell as a function of top cell thickness (For bottom Cell Composition: $Si_{0.98}Ge_{0.02}$)

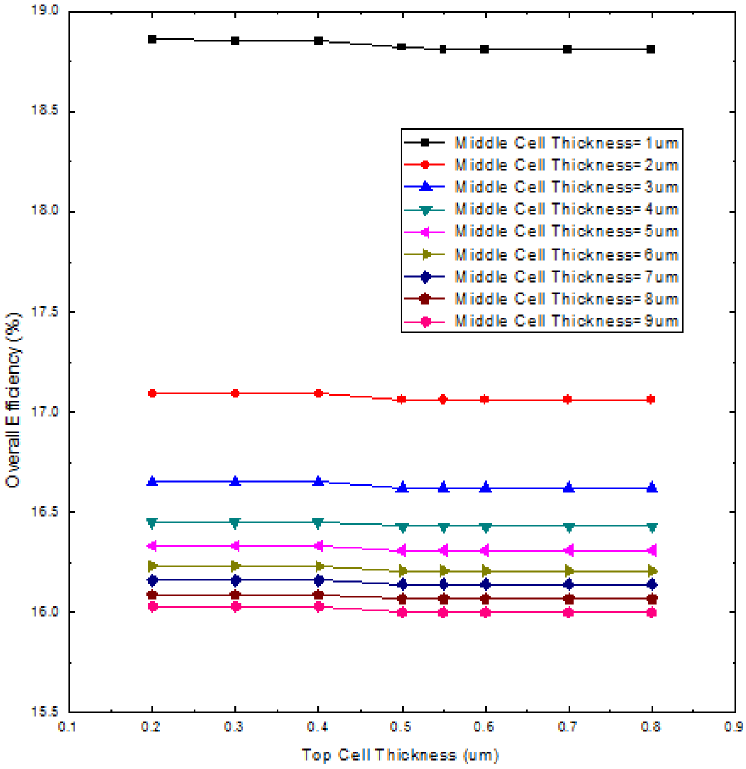

Figure 3.31 Overall efficiency of tandem solar cell as a function of top cell thickness (For bottom Cell Composition: $Si_{0.98}Ge_{0.02}$)

3.6 Optimizing additional layers

From table 3.2 it is seen that the maximum efficiency of 32.6% is achieved for bottom cell composition of $Si_{0.65}Ge_{0.35}$, for top cell thickness 0.40um and middle cell thickness 4um. Now the additional layers of this structure are further optimized and the results are observed. In the following figure we can see the overall cell efficiency as a function of the window layer thickness. As the window layer thickness increase, the efficiency of the cell is found to decrease. This can be explained by the fact that the window layer is used to reduce surface recombination and a thicker window layer would allow more area for recombination to occur thus producing an adverse effect. Similar explanation is true for the BSF layer thickness. In this case the thickness that gives maximum efficiency for window layer is 0.01um and BSF layer is 0.02um. The maximum efficiency obtained is 34.85%. The important parameters of the fully optimized triple junction solar cell is displayed in Table 3.3

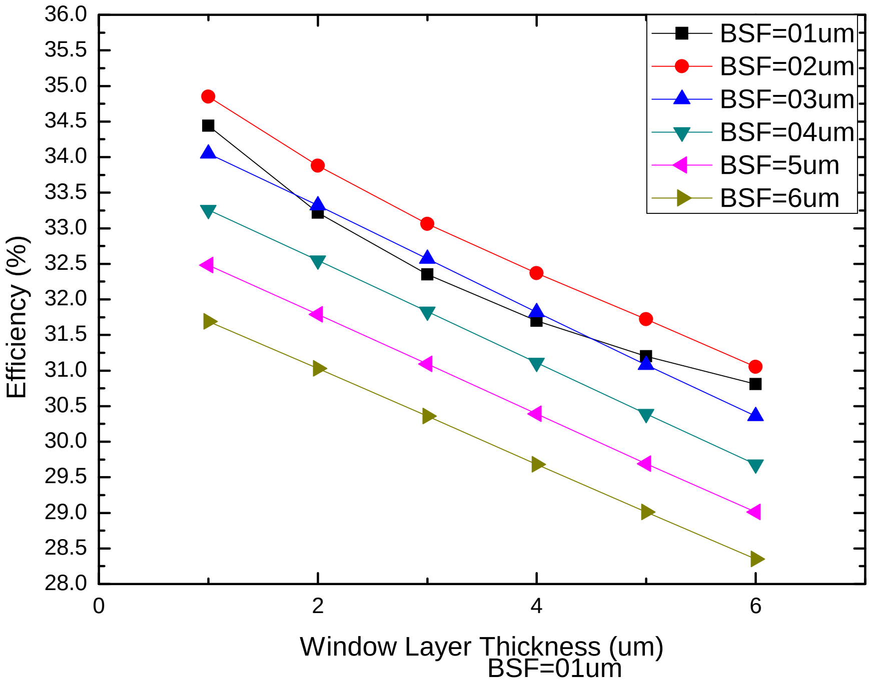

Figure 3.32 Overall Cell Efficiency as a function of Window Layer thickness

Bottom cell Composition	$Si_{0.65}Ge_{0.35}$
Efficiency	34.85%
Top Cell thickness	0.40um
Middle Cell thickness	4um
Bottom Cell Thickness	300um
Window layer thickness	0.01um
BSF layer thickness	0.02um

Table 3.3 Important parameters of the fully optimized triple junction solar cell

3.7 Ideal Condition

For this optimized cell, the efficiency was calculated under ideal conditions and an efficiency of 41.43% was achieved and the efficiency is plotted as a function of top cell thickness in Fig. 3.33

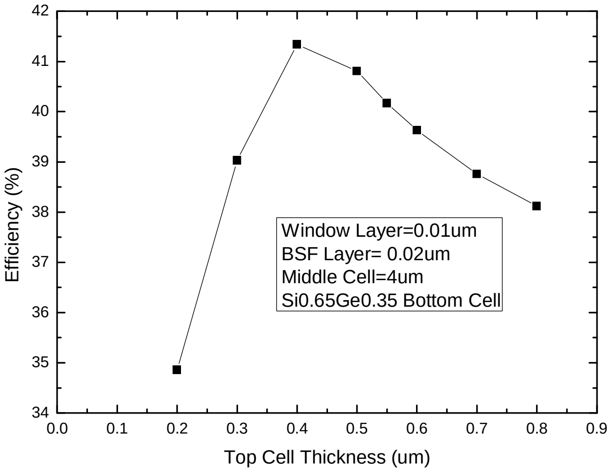

Figure 3.33 Overall Cell Efficiency as a function of top cell thickness under ideal condition

3.8 Summary

A new material for the bottom cell of a triple junction solar cell is introduced and its I-V characteristics are examined, first each subcell separately and then for the overall cell. Next the top and middle cell thickness are varied and its effects are studied. The dimensions are then optimized to get the maximum short circuit current possible and the bottom cell composition is varied its effect on overall cell efficiency is analyzed. Finally an optimum structure is selected with highest efficiency and its additional layers are further optimized to increase its efficiency even more. The final results are displayed in a table.

CHAPTER 4

CONCLUSION

4.1 Conclusion

In this work we analyzed and optimized a mechanically stacked triple junction InGaP/GaAs/Si_xGe_{1-x} solar cell using drift diffusion model. In our model, non idealities such as surface recombination, Shockley Reed Hall recombination and Auger recombination was taken into consideration. To reduce surface recombination a window layer was added on top of each subcell. Again to minimize carrier scattering a back surface field layer was also added at the bottom of each subcell. Finally at the top of the cell structure an anti reflection coating was added to avoid reflection of photons. Several physical parameters such as top cell thickness and middle cell thickness and material composition ($Si_{0.20}Ge_{0.80}$, $Si_{0.28}Ge_{0.72}$, $Si_{0.65}Ge_{0.35}$, $Si_{0.85}Ge_{0.15}$ and $Si_{0.98}Ge_{0.02}$) of the bottom cell were varied and I-V characteristics along with important parameters of solar cell performance was investigated. It was observed that with the increase in the top cell thickness, the top cell current increases, but the middle cell current significantly decreases due to shadowing effect, hence reducing overall cell performance. A similar trend is observed for the variation of middle cell thickness, which resulted in an increased middle cell current but decreased bottom cell current. So an appropriate selection of this cell thickness would result in an enhanced efficiency solar cell. The bottom cell composition was then altered and finally a maximum efficiency of 32.2% was obtained for $Si_{65}Ge_{35}$ bottom cell composition, top cell thickness of 0.4µm and middle cell thickness of 4µm. This is expected, since the band gap of $Si_{0.65}Ge_{0.35}$ is 1.14eV which is close to the ideal band gap for bottom cell material. It was evident from our simulation results that physical dimension of additional layers such as window layer and back surface field layer has significant impact on the cell efficiency. A thorough investigation of various physical dimensions was carried out which resulted in a maximum efficiency of 34.85% for a window layer thickness of 0.01µm and BSF layer thickness of 0.02µm. Finally for this optimized cell, an overall cell efficiency of 41.34% was obtained under ideal conditions

4.1 Suggestion for Future Works

This work can facilitate further study with this material system and device structure. The suggestions for future work are as follows:

- In this work mechanically stacked configuration of tandem cell was analyzed and designed for better efficiency. Monolithically integrated tandem cell, though comparatively complex and expensive, can be investigated and analyzed for study purpose.
- The defects caused by radiation effect in space can be modeled and included in design and optimization process of the tandem cell.
- The effect of temperature on solar cell performance can also be analyzed and this effect can be included in design and optimization process of tandem cell.
- In this work 1 sun illumination was considered. The structure can be studied in CPV (Concentrated Photovoltaic s) system and optimized for this environment.

REFERENCES

[1] Becquerel, A. E. "On electric effects under the influence of solar radiation." *CR Acad. Sci* 9 (1839): 711-4.

[2] Chapin, Daryl M., C. S. Fuller, and G. L. Pearson. "A new silicon p-n junction photocell for converting solar radiation into electrical power." *Journal of Applied Physics* 25 (1954): 676-677.

[3] Shockley, William, and Hans J. Queisser. "Detailed balance limit of efficiency of p-n junction solar cells." *Journal of applied physics* 32, no. 3 (1961): 510-519.

[4] Yastrebova, Natalya V. "High-efficiency multi-junction solar cells: Current status and future potential." *Solar Energy* (2007).

[5] Zhang Y. H, Wu S. N., Ding D., Yu S. Q., and Johnson S.R., "A proposal of monolithicly integrated multijunction solar cells using lattice-matched II/VI and III/V semiconductors," *Proc. of Photovoltaic Specialists Conference, 2008. PVSC'08. 33rd IEEE*, pp. 1-5, May 2008.

[6] Gnilenko A. B., and Plaksin S. V, "Mechanically Stacked Triple-junction GaInP/GaAs/Si Solar Cell Simulation," *J. Nano and Electron. Phys.*, vol. 5. no. 4, p. 04057, Jan 2014

[7] Leit .e MS., Woo ,.L .R Munday ,.N .J Hong ,.D .W Mesropian ,.S Law ,.C .D and Atwater .A .H ,"Towards an optimized all lattice-matched InAlAs/InGaAsP/InGaAs multijunction solar cell with efficiency> 50%," *Appl. Phys. Lett.,* vol. 102, no. 3, p. 033901, Jan2013

[8] Stan M., Aiken D., Cho B., Cornfeld A., Diaz J., Ley V., Korostyshevsky A., Patel P., Sharps P., and Varghese T., "Very high efficiency triple junction solar cells grown by MOVPE," *.J Crystal Growth* .vol ,310, no. 23, .p5204-5208, Nov2008

[9] Hermle M., Letay G. , Philipps S. P. and Bett A. W., "Numerical simulation of tunnel diodes for multi-junction solar cells," *Progress in Photovoltaics: Research and Applications*.vol , 16, no. 5, Aug ,418-409 .pp2008.

[10] Yamaguchi M., "Multi-junction solar cells and novel structures for solar cell applications, " *Physica E: Low-dimensional Systems and Nanostructures* .vol ,14, no. 1, .pp 82002Apr ,90-4

[11] Friedman D. J., "Progress and challenges for next-generation high-efficiency multijunction solar cells," *Current Opinion in Solid State and Materials Science* .vol , 14, no. 6, .2010Dec ,138-131 .pp

[12] J. M. Olson , S. R. Kurtz , A. E. Kibbler and P. Faine "A 27.3% Efficient Ga0.5ln0.5P/GaAs Tandem Solar Cells", *Appi. Phys. Lett.*, vol. 56, pp.623 1990

[13] Bertness, K. A., Sarah R. Kurtz, D. J. Friedman, A. E. Kibbler, C. Kramer, and J. M. Olson. "29.5%-efficient GaInP/GaAs tandem solar cells." *Applied Physics Letters* 65, no. 8 (1994): 989-991.

[14] King R. R., Law D. C. , Edmondson K. M., Fetzer C. M., Kinsey G. S. ,Yoon H. , Sherif R. A. ,and Karam N. H., "40% efficient metamorphic GaInP/GaInAs/Ge multijunction solar cells," *ApL .Phys .lett* .vol ,. 90, no. 18, .p 1835162007May ,.

[15] Geisz J. F., Kurtz S., Wanlass M. W. , Ward J. S. , Duda A. , Friedman D. J. , Olson J. M., McMahon W. E., Moriarty T. E. and Kiehl J. T., "High-efficiency GaInP/GaAs/InGaAs triple-junction solar cells grown inverted with a metamorphic bottom junction, " *Appl. Phys. Lett* .olv ,.91, no. 2, .p023502 , July2007

[16] King, R. Richard, A. Boca, W. Hong, X. Q. Liu, D. Bhusari, D. Larrabee, K. M. Edmondson et al. "Band-gap-engineered architectures for high-efficiency multijunction concentrator solar cells." In *24th European Photovoltaic Solar Energy Conference and Exhibition, Hamburg, Germany*, vol. 21. P 55 2009.

[17] Kurtz S., Myers D. and Olson J.M., "Projected performance of three-and four-junction devices using GaAs and GaInP, " *Conference Record IEEE Photovoltaic Specialists Conference*, vol. 26, pp. 875-878 Sep ,1997

[18] M. Wiemer, V. Sabnis, H. Yuen, “43.5% efficient lattice matched solar cells” *PROCEEDINGS OF SPIE*, vol 8108 04, 2011

[19] Zahler, James M., Katsuaki Tanabe, Corinne Ladous, Tom Pinnington, Frederick D. Newman, and Harry A. Atwater. "High efficiency InGaAs solar cells on Si by InP layer transfer." *Applied physics letters* 91, no. 1 (2007): 012108.

[20] Szabo, N., B. E. Sağol, U. Seidel, K. Schwarzburg, and T. Hannappel. "InGaAsP/InGaAs tandem cells for a solar cell configuration with more than three junctions." *physica status solidi (RRL)-Rapid Research Letters* 2, no. 6 (2008): 254-256.

[21] Kurtz S., Johnston S., and Branz H.M., "Capacitance-spectroscopy identification of a key defect in N-degraded GalnNAs solar cells, "*Appl. Phys. Let* .vol ,*.t*86, no. 11 .p , ,113506 July2005.

[22] Kidd, P., D. J. Dunstan, H. G. Colson, M. A. Louren, A. Sacedo, F. Gonza, L. Gonza et al. "Comparison of the crystalline quality of step-graded and continuously graded InGaAs buffer layers." *Journal of crystal growth* 169, no. 4 (1996): 649-659.

[23] Ahrenkiel, S. P., M. W. Wanlass, J. J. Carapella, L. M. Gedvilas, B. M. Keyes, R. K. Ahrenkiel, and H. R. Moutinho. "Characterization survey of GaxIn1− xAs/InAsyP1− y double heterostructures and InAsyP1− y multilayers grown on InP." *Journal of electronic materials* 33, no. 3 (2004): 185-193.

[24] . Wanlass, Mark W., S. P. Ahrenkiel, R. K. Ahrenkiel, D. S. Albin, J. J. Carapella, A. Duda, J. F. Geisz et al. "Lattice-mismatched approaches for high-performance, III-V photovoltaic energy converters." In *Photovoltaic Specialists Conference, 2005. Conference Record of the Thirty-first IEEE*, pp. 530-535. IEEE, 2005.

[25] Wanlass, Mark, Phil Ahrenkiel, David Albin, Jeff Carapella, Anna Duda, Keith Emery, Daniel Friedman et al. "Monolithic, ultra-thin GaInP/GaAs/GaInAs tandem solar cells." In *Photovoltaic Energy Conversion, Conference Record of the 2006 IEEE 4th World Conference on*, vol. 1, pp. 729-732. IEEE, 2006

[26] Yamaguchi, Masafumi, and Chikara Amano. "Efficiency calculations of thin-film GaAs solar cells on Si substrates." *Journal of applied physics* 58, no. 9 (1985): 3601-3606.

[27] King, R. R., N. H. Karam, J. H. Ermer, M. Haddad, P. Colter, T. Isshiki, H. Yoon et al. "Next-generation, high-efficiency III-V multijunction solar cells." In*Photovoltaic Specialists Conference, 2000. Conference Record of the Twenty-Eighth IEEE*, pp. 998-1001. IEEE, 2000.

[28] Dimroth, F., U. Schubert, and A. W. Bett. "25.5% efficient Ga/sub 0.35/In/sub 0.65/P/Ga/sub 0.83/In/sub 0.17/As tandem solar cells grown on GaAs substrates." *Electron Device Letters, IEEE* 21, no. 5 (2000): 209-211.

[29] C. L. Andre, A. Khan, M. Gonzalez, M. K. Hudait, E. A. Fitzgerald, J. A. Carlin, M. T. Currie, C. W. Leitz, T. A. Langdo, E. B. Clark, D. M. Wilt, and S. A. Ringel," Single-junction InGaP/GaAs solar cells grown on Si substrates with SiGe buffer layers" Proceedings of the 29th IEEE PV Specialists Conference, _IEEE, Piscataway, NJ, 2002_, p. 1043

[30] Takamoto, Tatsuya, Takaaki Agui, Kazutaka Kamimura, and Minoru Kaneiwa. "Multijunction solar cell technologies-high efficiency, radiation resistance, and concentrator applications." In *Photovoltaic Energy Conversion, 2003. Proceedings of 3rd World Conference on*, vol. 1, pp. 581-586. IEEE, 2003.

[31] King, R. R., D. C. Law, C. M. Fetzer, R. A. Sherif, K. M. Edmondson, S. Kurtz, G. S. Kinsey et al. "Pathways to 40%-efficient concentrator photovoltaics." In*Proc. 20th European Photovoltaic Solar Energy Conference*, pp. 10-11. 2005.

[32] King, Richard R., Christopher M. Fetzer, Daniel C. Law, Kenneth M. Edmondson, Hojun Yoon, Geoffrey S. Kinsey, Dimitri D. Krut et al. "Advanced III-V multijunction cells for space." In *Photovoltaic Energy Conversion, Conference*

Record of the 2006 IEEE 4th World Conference on, vol. 2, pp. 1757-1762. IEEE, 2006.

[33] King, R. R., R. A. Sherif, D. C. Law, J. T. Yen, M. Haddad, C. M. Fetzer, K. M. Edmondson et al. "New horizons in III-V multijunction terrestrial concentrator cell research." In *21st European PV Solar Energy Conference, Dresden*. 2006.

[34] Fontcuberta i Morral, A., J. M. Zahler, Harry A. Atwater, S. P. Ahrenkiel, and M. W. Wanlass. "InGaAs/InP double heterostructures on InP/Si templates fabricated by wafer bonding and hydrogen-induced exfoliation." *Applied physics letters* 83, no. EPFL-ARTICLE-149094 (2003): 5413.

[35] Archer, Melissa J., Daniel C. Law, Shoghig Mesropian, Moran Haddad, Christopher M. Fetzer, Arthur C. Ackerman, Corinne Ladous, Richard R. King, and Harry A. Atwater. "GaInP⁄ GaAs dual junction solar cells on Ge⁄ Si epitaxial templates." *Applied Physics Letters* 92, no. 10 (2008): 103503.

[36] Kim, Hyung Chul, Vasilis Fthenakis, Jun-Ki Choi, and Damon E. Turney. "Life cycle greenhouse gas emissions of thin-film photovoltaic electricity generation." *Journal of Industrial Ecology* 16, no. s1 (2012): S110-S121.

[37] Candelise, Chiara, Mark Winskel, and Robert JK Gross. "The dynamics of solar PV costs and prices as a challenge for technology forecasting." *Renewable and Sustainable Energy Reviews* 26 (2013): 96-107.

[38] Zweibel, Ken, James Mason, and Vasilis Fthenakis. "A solar grand plan."*Scientific American* 298, no. 1 (2008): 64-73.

[39] Pulfrey, L.D. (1978). *Photovoltaic Power Generation*. New York: Van Nostrand Reinhold Co. ISBN 9780442266400

[40] Milliron, Delia J., Ilan Gur, and A. Paul Alivisatos. "Hybrid organic–nanocrystal solar cells." *Mrs Bulletin* 30, no. 01 (2005): 41-44.

[41] D. Neaman. *An Introduction to Semiconductor Devices*, New York, NY: McGraw Hill, 2006.

[42] Narasimha, Shreesh, Ajeet Rohatgi, and A. W. Weeber. "An optimized rapid aluminum back surface field technique for silicon solar cells." *Electron Devices, IEEE Transactions on* 46, no. 7 (1999): 1363-1370.

[43] Eades, Wendell D., and Richard M. Swanson. "Calculation of surface generation and recombination velocities at the Si-SiO2 interface." *Journal of Applied physics* 58, no. 11 (1985): 4267-4276.

[44] Fossum, Jerry G. "Physical operation of back-surface-field silicon solar cells."*IEEE Transactions on Electron Devices* 24 (1977): 322-325.

[45] Vasileska, Dragica. "Drift-Diffusion Model: Introduction." *Arizona State University:[sn]* (2006).

[46] Atlas Silvaco, *Atlas User’s Manual International*, Vol. 1–2, 2007.

[47] *ATLAS User's Manual*, vols. 1-2, software version 5.6.0.R, Silvaco International, Santa Clara, CA, 2012.